Spray dispersion regimes following atomization in a turbulent co-axial gas jet

P D Huck, R Osuna-Orozco, Nathanaël Machicoane, A Aliseda

Spray dispersion regimes following atomization in a turbulent co-axial gas jet

Journal:	*Journal of Fluid Mechanics*
Manuscript ID	JFM-21-S-0668.R2
Manuscript Type:	JFM Papers
Date Submitted by the Author:	18-Oct-2021
Complete List of Authors:	Huck, Peter; The George Washington University, Aerospace and Mechanical Engineering Osuna-Orozco, Rodrigo; University of Washington, Department of Mechanical Engineering Machicoane, Nathanael; Universite Grenoble Alpes, LEGI Aliseda, Alberto; University of Washington, Department of Mechanical Engineering
JFM Keywords:	Multiphase flow < Multiphase and Particle-laden Flows, Particle/fluid flows < Multiphase and Particle-laden Flows, Aerosols/atomization < Drops and Bubbles
Abstract:	A canonical co-axial round-jet two-fluid atomizer where atomization occurs over a wide range of momentum ratios: M=1.9-376.4 is studied. The near field of the spray, where the droplet formation process takes place, is characterized and linked to the droplet distribution in the far field via turbulent dispersion. Counterintuitively, our results indicate that in the low-momentum regime, increasing the momentum in the gas-phase leads to less droplet spreading. A critical momentum ratio of the order of M_c=50, that separates this regime from the more intuitive high-momentum/fast-spreading one, is found in both the near and far-field. A phenomenological model is proposed that determines the susceptibility of droplets to disperse beyond the nominal extent of the gas phase based on a critical Stokes number, $St=\tau_p/T_E=1.9$, formulated based on the local Eulerian large scale eddy turn-over time, T_E, and the droplets' response time, τ_p. A two-dimensional phase-space summarizes the extent of these different regimes in the context of spray characteristics found in the literature.

Spray dispersion regimes following atomization in a turbulent co-axial gas jet

P. D. Huck [1], R. Osuna-Orozco [1], N. Machicoane[1,2], A. Aliseda[1]†.

[1]University of Washington - Department of Mechanical Engineering, Seattle, WA, USA

[2]University of Grenoble Alpes, CNRS, Grenoble INP, LEGI, 38000 Grenoble, France

(Received xx; revised xx; accepted xx)

A canonical co-axial round-jet two-fluid atomizer where atomization occurs over a wide range of momentum ratios: $M = 1.9 - 376.4$ is studied. The near field of the spray, where the droplet formation process takes place, is characterized and linked to droplet dispersion in the far field of the jet. Counterintuitively, our results indicate that in the low-momentum regime, increasing the momentum in the gas-phase leads to less droplet dispersion. A critical momentum ratio of the order of $M_c = 50$, that separates this regime from a high-momentum one with less dispersion, is found in both the near and far-field. A phenomenological model is proposed that determines the susceptibility of droplets to disperse beyond the nominal extent of the gas phase based on a critical Stokes number, $St = \tau_p/T_E = 1.9$, formulated based on the local Eulerian large scale eddy turn-over time, T_E, and the droplets' response time, τ_p. A two-dimensional phase-space summarizes the extent of these different regimes in the context of spray characteristics found in the literature.

Key words:

1. Introduction

Liquid droplet production by a jet-like momentum source is relevant in industrial and biological processes such as combustion efficiency in liquid fuel engines (Hardalupas *et al.* 1990; Hardalupas & Whitelaw 1993), cost constraints in metal powder production (Ünal 1989) for additive manufacturing, and aerosol transport during human exhalations (Balachandar *et al.* 2020; Abkarian *et al.* 2020). The resulting poly-disperse collection of droplets, or *spray*, interact with the turbulence in the jet far-field. A unified framework is presented where the initial droplet production mechanisms of an air-water spray are connected with the subsequent dispersion in the jet far field.

Studies of the shear layer in coaxial round jets where a central low momentum liquid jet (density: ρ_ℓ, velocity: U_ℓ) is surrounded by high momentum gas (ρ_g, U_g) jet (see Lasheras & Hopfinger (2000); Dumouchel (2008) for extensive reviews) emphasize the role of momentum balance across the liquid-gas interface in determining the nature of atomization. The momentum ratio,

$$M = \rho_g u_g^2/(\rho_\ell u_\ell^2), \tag{1.1}$$

is an indicator of the momentum balance that sustains the advection of shear-layer vortices at a velocity U_c such that $U_c/U_\ell \sim M^{1/2}$ (Dimotakis 1986). A critical value of the momentum ratio has been observed, of the order of $M = 50$, where the inner jet's momentum is not sufficient to

† Email address for correspondence: aaliseda@u.washington.edu

balance that of the outer jet and a recirculating vortex core is established near the nozzle, which truncates the central jet (Rehab *et al.* 1997; Favre-Marinet *et al.* 1999; Lasheras & Hopfinger 2000). Synchrotron radiography measurements implicate this recirculating vortex in the various break-up regimes beyond the critical momentum ratio in a liquid spray (Machicoane *et al.* 2019). These processes are often coupled with large-scale instabilities causing strong lateral excursions of the liquid jet known as flapping "flapping" (Delon *et al.* 2018) or "dilatational waves" resulting in clustered break-up of a high momentum liquid core (Engelbert *et al.* 1995; Kumar & Sahu 2020).

Once formed, droplets are advected into the far-field of the jet where droplet inertia is the fundamental parameter governing dispersion. These processs are parameterized by the ratio of particle response time τ_p and fluid characteristic time scale τ_f, known as the Stokes number:

$$St = \tau_p/\tau_f. \tag{1.2}$$

Much of what is known of droplet dispersion has been studied in the context of monodisperse particle-laden jets (PLJ). Lau & Nathan (2014, 2016) observed that dispersion in the far field of the jet was reduced for increasing St, and linked this effect to the initial conditions. In particular, a competition between the Saffman force (Saffman 1965) tending to accumulate large St particles near the centerline and turbophoresis (Reeks 1983) which tends to accumulate small St particles near the jet edges, was observed at the jet nozzle. This St-dependent phenomenon is fundamentally different than the interfacial instabilities described above and lead to non-trivial differences in initial conditions governing the evolution of the PLJ and a spray.

Despite these differences, interaction of the dispersed phase with large scale vortices present in the near and far fields of shear-driven flows (Brown & Roshko 1974; Yule 1978) are fundamental in both sprays and PLJ. Early modeling efforts by Chung & Troutt (1988) emphasized the enhanced dispersion of particles interacting with vortices when the particle's response time τ_p is of the same order as the eddies' characteristic timescale τ_f. When the particle Stokes number was of the order of unity enhanced dispersion was demonstrated experimentally (Longmire & Eaton 1992; Lazaro & Lasheras 1992*a*,*b*) as well as numerically (Sbrizzai *et al.* 2004; Picano *et al.* 2010).

Understanding the dispersion of a spray is fundamental for practical applications where mass, momentum, and heat transfer as well as chemical reactions may be sensitive to local droplet size as well as the presence of other droplets. Despite the strong qualitative differences in droplet-size profiles observed using interferometric techniques (Eroglu & Chigier 1991; Zaller & Klem 1991; Hardalupas & Whitelaw 1993, 1994; Engelbert *et al.* 1995), no consensus exists for estimating the shape of the spray based on physically meaningful parameters of the atomization and dispersion regimes encountered. The present study establishes how known mechanisms governing the formation of droplets in the near-field of a canonical co-axial atomizer influence the subsequent dispersion of these droplets in the far field.

The paper organization is as follows. Section 2 describes the experimental methods used. The gas-phase is characterized in section 3. In section 4, we describe the break-up mechanisms of the liquid relevant to the question of dispersion in the far-field. We present the structure of the dispersed liquid phase in section 5. A model is presented in section 6 to account for the observed evolution of the spray. Droplet-size profiles are presented are put into context with regards to sprays found in the literature with a phase space diagram in section 7. A discussion and conclusions follow in section 8.

2. Methods

The spray used here is produced by a coaxial turbulent gas jet atomizing a central laminar liquid jet, as sketched in figure 1(a). A fully developed Poiseuille flow in the central channel exits the

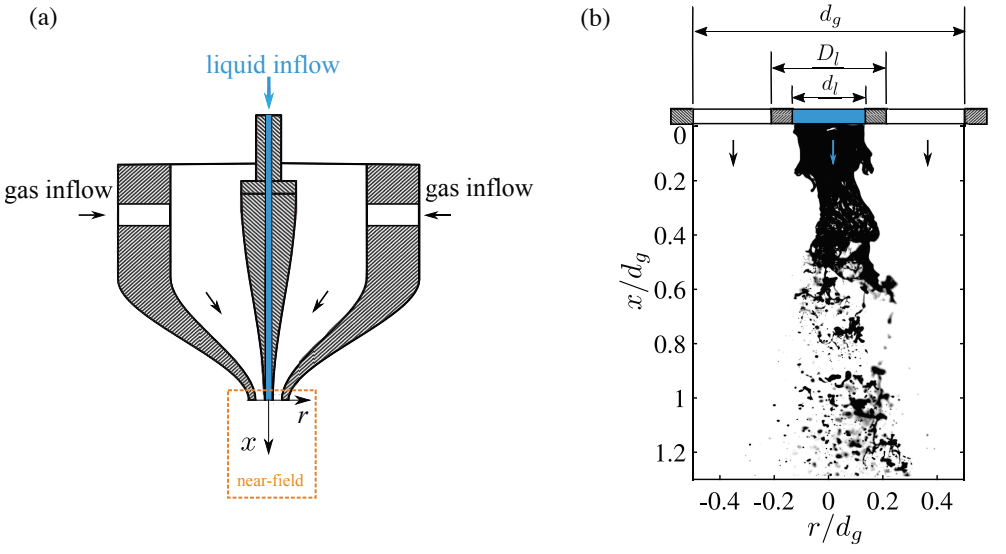

FIGURE 1. Experimental overview (a) Co-axial nozzle geometry where black (blue) arrows illustrate the flow of gas (liquid). The orange dashed box illustrates the near-field region observed with back-lit imaging.(b) Back-lit image illustrating nozzle geometry and atomization process for experiment (1a) in table 1. The outer gas diameter d_g = 1cm, the outer liquid diameter D_ℓ = 3 mm, and the inner liquid diameter d_ℓ = 2 mm.

nozzle forming a liquid jet which comes into contact with co-flowing gas jet leading to atomization (figure 1 b). The diameter of the co-axial gas jet is d_g while the inner diameter d_ℓ characterizes the central laminar liquid jet. The liquid velocity is given by $U_\ell = Q_\ell/A_\ell$ where $A_\ell = \pi d_\ell^2/4$, giving a liquid Reynolds number of $Re = U_\ell d_\ell/\nu_\ell$, where ν_ℓ is the kinematic viscosity at the laboratory temperature of 25°C. Four gas inlets are arranged perpendicular to the axis of the liquid flow resulting in a gas flow with zero angular momentum. The gas inlets supply the nozzle with a volume flow rate Q_g, which exits through an annular cross-section $A_g = \pi(d_g^2 - D_\ell^2)/4$, resulting in a gas velocity of $U_g = Q_g/A_g$ and a Reynolds number $Re_g = U_g d_g/\nu_g$. Additionally, the ratio of the dynamic pressure in the gas and liquid phases, known as the momentum ratio is given by $M = \rho_g U_g^2/(\rho_\ell U_\ell^2)$. The Weber number based on the average exit velocities is: $We = \rho_g(U_g - U_\ell)^2 d_\ell/\sigma$, where σ is the liquid-gas interfacial surface tension. The liquid mass loading, which compares the liquid to gas mass fluxes, is given by: $m = \rho_\ell A_\ell U_\ell/(\rho_g A_g U_g)$. This experimental facility has been characterized previously (Machicoane *et al.* 2019, 2020) in a similar range of parameters as those presented here (table 1).

The experimental results presented here are obtained by three techniques: Phase Doppler Interferometry (PDI), Laser Doppler Velocimetry (LDV), and Direct Imaging (DI). DI was accomplished by backlighting with a high powered LED either in the optical axis of a high speed camera (Phantom V.12, Vision Research), which resulted in back-lit imaging (figure 3a,b) or at an angle of 30° where first-order refraction is the dominant forward-scattering mode from water droplets (fig. 3c,d). Back-lit imaging was done with a magnification of 0.77X using a Tamron 180mm Macro lens with an exposure time of $0.3\mu s$ in order to capture the behavior of the atomization at the nozzle. The forward-scattering imaging was done with a Zeiss 100mm Macro lens ($49\mu s$ exposure time) and had a much lower magnification (0.07X) in order to capture the dynamics of a large portion of the spray.

Phase Doppler Interferometry (PDI) and Laser Doppler Velocimetry (LDV) were used to gather point-wise, simultaneous measurements of radial and axial velocities as well as droplet diameters. The TSI LDV/PDI system (FSA4000 Signal Processor, PDM1000 Photo Detector Module) was

U_g (m/s)	U_ℓ (m/s)	Re_g	Re_ℓ	M	We	m	Series	Technique
34.9	0.5	22400	1170	5.3	38.9	0.56	1a	DI
43.2	0.5	27700	1170	8.0	59.5	0.45	1b	DI
51.3	0.5	32900	1170	11.3	84.5	0.38	1c	DI
64.1	0.5	41100	1170	17.7	132.6	0.30	1d	DI
86.1	0.5	55200	1170	31.8	239.7	0.23	1e	DI
296.1	0.5	189800	1170	376.4	2864.7	0.07	1f	DI
76.7	0.5	49200	1170	25.3	190.3	0.25	2a	DI/LDV/PDI
95.6	0.5	61300	1170	39.2	296.3	0.20	2b	DI/LDV/PDI
114.3	0.5	73300	1170	56.0	424.0	0.17	2c	DI/LDV/PDI
137.6	0.5	88200	1170	81.2	615.7	0.14	2d	DI/LDV/PDI
202.9	0.5	130000	1170	176.6	1342.2	0.10	2e	DI/LDV/PDI
95.6	0.5	61300	1170	39.2	292.7	0.20	3a	DI/LDV/PDI
95.6	1.5	61300	3260	5.1	287.0	0.57	3b	DI/LDV/PDI
95.6	2.4	61300	5330	1.9	281.3	0.93	3c	DI/LDV/PDI

TABLE 1. Flow parameters: gas Reynolds number: Re_g, liquid Reynolds number: Re_ℓ, momentum ratio: M, Weber number: We, mass loading: m. The gas (liquid) density at 25°C: $\rho_g = 1.18$ kg/m^3 ($\rho_\ell = 996.9$ kg/m^3), gas (liquid) dynamic viscosity: $\nu_g = 1.56 \times 10^{-5}$ m^2/s ($\nu_\ell = 0.90 \times 10^{-6}$ m^2/s), the liquid-gas interface surface tension $\sigma = 72.0$ mN/m.

operated in forward scattering with first-order refraction, the dominant mode at an observation angle of $\theta = 60°$ for series 2(a-d) (operational details in Table 2) and in backward scattering, with reflection the dominant mode, at an observation angle $\theta = 150°$ for series 2(e) and 2(a-c). The FSA provided an estimation of the signal-to-noise ratio as well as the number of cycles adequate for phase measurements for the incoming Doppler bursts. In series 2(a-e) the ratio of bursts satisfying these criteria to the total number of bursts was [77%, 69%, 58%, 60%, 50%] and were deemed sufficiently high for quality measurements. Standard intensity and phase validation algorithms were followed to ensure further accuracy of the droplet size measurements (Albrecht *et al.* 2003).

An estimation of the probe volume viewed by the receiving probe was critical to properly determine the volume flux density and volume fraction in the experiments. An afocal relay system with an interchangeable collimating lens ($f_c = [300,\ 750]\mu$m) and imaging lens ($f_i = 250\ \mu$m) was implemented to vary the magnification ($\beta = -f_i/f_c$). At the beam crossing the probe volume is approximately a prolate spheroid, however the use of a spatial filter ($s = 150\mu$m) truncates the volume along the major axis and permits a well-defined probe length. Due to the collection angles employed, the probe length was effectively longer than the slit by a factor of $1/\sin(\theta)$ and after accounting for the magnification employed, the probe length could be calculated precisely as $L = s/|\beta|\sin(\theta)$. The product of the droplet longitudinal velocity and gate-time (*i.e.* residence time in the probe volume) gives a path length ℓ that is dependent on the droplet diameter, due to the gaussian nature of the laser beam (Albrecht *et al.* 2003). In flows where the magnitude of the droplet velocity is dominated by the longitudinal velocity, such as in round jets without swirl, droplet trajectory effects in the probe volume are negligible and ℓ is essentially the diameter of the cylinder of length L. The diameter-dependent probe cross-sectional area is then:

$$\mathcal{A} = \frac{\ell L}{|\beta| \sin\theta}. \tag{2.1}$$

Green Laser mW	Blue Laser mW	$1/\lvert\beta\rvert$ -	θ deg	s μm	L mm	Experimental Series -
275	400	3.0	60	150	0.520	2a
275	400	3.0	60	150	0.520	2b
375	400	3.0	60	150	0.520	2c
275	400	1.2	60	150	0.208	2d
525	550	3.0	150	150	0.900	2e
275	400	3.0	150	150	0.900	3a
275	400	3.0	150	150	0.900	3b
275	400	3.0	150	150	0.900	3c

TABLE 2. Parameters for the PDI. Magnification of the receiving optics: $\beta = -f_i/f_c$ with the collimating (imaging) lens focal length f_c (f_i), θ is the observation angle. The spatial filter (slit) width : s . Projected probe length: $L = s/|\beta| \sin(\theta)$.

and the probe volume is:

$$\mathcal{V} = \frac{\pi}{4} \frac{\ell^2 L}{|\beta| \sin\theta}. \tag{2.2}$$

A curve fit of path length ℓ as a function of the binned diameter is obtained during the data post-processing for the different laser power and magnification combinations in table 2 to obtain the relevant probe area and volume.

3. Gas phase

In order to characterize the gas phase, the PDI data was conditioned for the smallest droplet diameters (roughly $d = 1\mu m$). We calculate a Stokes number based on the nozzle conditions:

$$St_d = \frac{\tau_p}{d_g/U_g} \tag{3.1}$$

where $\tau_p = \rho_\ell d^2/(18\rho_g \nu_g)$ is the droplet response time. We find that these droplets have Stokes numbers in the range $St_d = [0.02 - 0.06]$ for the range of Reynolds numbers considered here. The length (velocity) scale of the jet increases (decreases) with axial distance, x, leading to a time scale that increase as x^2. Therefore, the Stokes number of these droplets decreases quickly with axial distance from the nozzle, supporting the assumption that these droplets act as flow tracers. This claim is confirmed, *a posteriori*, by the comparisons presented below of the first and second order statistics against the well-known self-similar turbulent round jet.

The downstream evolution of the inverse average centerline velocity $U_0(x) = \langle U(x, r = 0)\rangle$ normalized by nozzle velocity U_g is plotted in 2(a). Linear increase indicates that $U_0 \propto (x - x_0^{\langle U\rangle})^{-1}$. This evolution can be approximated by

$$\frac{U_g}{U_0} = \frac{1}{B_{\langle U\rangle}} \frac{x - x_0^{\langle U\rangle}}{d_g}, \tag{3.2}$$

where $B_{\langle U\rangle}$ determines the average velocity decay rate and $x_0^{\langle U\rangle}$ is the virtual origin, which are given in table 3. The evolution of the average velocity is in agreement with the experiments of (Panchapakesan & Lumley 1993) given by the dashed line in figure 2(a) with $B_{\langle U\rangle} = 6.06$

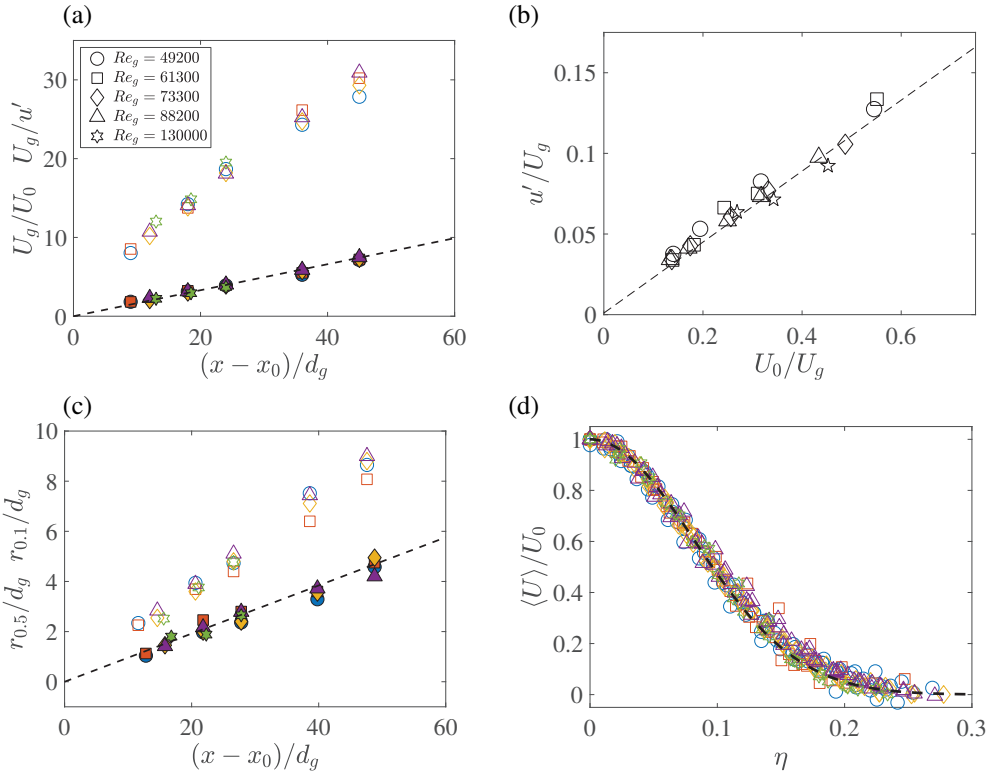

FIGURE 2. Gas phase evolution for $Re_g = [49200 - 130000]$. (a) Inverse of the average velocity (solid symbols, U_j/U_0) and of the fluctuating velocity (open symbols, U_g/u') in the axial direction. Dashed lines are the data from (Panchapakesan & Lumley 1993). (b) Centerline fluctuations as a function of average velocity for all Re_g and positions . Turbulence intensity (u'/U_0) is roughly 22% as determined by linear fit (dashed line, $R^2 = 0.97$) . (c) Location of the half-width (50^{th} percentile) of the average axial velocity in the radial profile (closed symbols, $r_{0.5}/d_g$). Dashed lines is the data from (Panchapakesan & Lumley 1993). Location of the ten-percent width (10^{th} percentile) of the average axial velocity in the radial profile (open symbols, $r_{0.1}/d_g$). (d) Self-similar axial velocity profiles fit by equation 3.5 (dashed black line) for all positions and Re_g.

and $x_0^{\langle U \rangle} = 0$. The evolution of the centerline fluctuating velocity is also plotted in figure 2(a), showing its inverse increasing approximately linearly (can be described by an equation analogous to 3.2 with constants $B_{u'}$ and $x_0^{u'}$ given in table 3). However, the scatter in the fluctuating velocity data is stronger than in the average velocity due to the role of droplet inertia in following gas-phase velocity fluctuations as St_d increases. Decay in u' is slightly stronger for higher Re_g due to small but non-zero inertia of the tracers, especially near the nozzle. Nevertheless, the turbulence intensity $u'/\langle U \rangle$ reaches a (roughly) constant value of 22% given by the slope of figure 2(b) and is in agreement with values found in the literature (Panchapakesan & Lumley 1993; Wygnanski & Fiedler 1969). The linear proportionality between u' and U_0 indicate that the jet is self-similar in the regions investigated.

As a consequence of the decay in the centerline velocity with x, the width of the jet is required to evolve linearly with x, to conserve momentum. The half-width ($r_{0.5}$) is defined as the position for which $\langle U(x, r = r_{0.5}) \rangle = 0.5U_0$. Similarly, the ten-percent width ($r_{0.1}$) is defined as $\langle U(x, r = r_{0.1}) \rangle = 0.1U_0$. In figure 2(c) both are seen to evolve linearly as expected in a momentum-driven jet. An important difference between these two metrics is that $r_{0.5}$ sits in the region characterized by outward radial expansion (positive average radial velocity) of the jet while $r_{0.1}$ lies in the region

$B_{\langle U\rangle}$ -	$x_0^{\langle U\rangle}$ (cm)	$B_{u'}$ -	$x_0^{u'}$ (cm)	$S_{0.5}$ -	$x_0^{0.5}$ (cm)	$S_{0.1}$ -	$x_0^{0.1}$ (cm)	$\theta_{0.5}^{U}$ (deg)	$\theta_{0.1}^{U}$ (deg)	C -
6.7	-2.4	1.7	-6.4	0.093	-3.8	0.182	-2.6	10.6	20.6	75.0

TABLE 3. Table of constants used to characterize the gas-phase axial velocity profiles in a two-phase jet for $Re_g = [49200 - 130000]$. The decay rate of the average velocity (fluctuations) is given by $B_{\langle U\rangle}$ ($B_{u'}$) with the relevant virtual origins $x_0^{\langle U\rangle}$ ($x_0^{u'}$). The spreading rate of the half-width (ten-percent width) is given by $S_{0.5}$ ($S_{0.1}$) with the relevant virtual origins $x_0^{0.5}$ ($x_0^{0.1}$). The opening angle defined by the half-width (ten-percent width) is $\theta_{0.5}$ ($\theta_{0.1}$). Average axial velocity of the form in equation 3.5 is determined by C.

characterized by jet entrainment (negative average radial velocity) (Panchapakesan & Lumley 1993; Wygnanski & Fiedler 1969). We note that the latter definition will be useful in quantifying droplet dispersion. We can calculate the spreading rate based on the half-width by:

$$r_{0.5} = S_{0.5}\left(x - x_0^{0.5}\right) \tag{3.3}$$

from which the spreading angle is calculated,

$$\theta_{0.5} = 2\tan^{-1}(S_{0.5}). \tag{3.4}$$

Both give agreement with values found in the literature for the spreading rates; the data from (Panchapakesan & Lumley 1993) is plotted in figure 2(c) in dashed lines with $x_0^{0.5} = 0$ and $S_{0.5} = 0.096$. Analogous quantities for the ten-percent width, $S_{0.1}$ and $\theta_{0.1}$ are reported in table 3 for the present experiments.

The evolution of the centerline mean velocity and radial spreading indicate self-similarity of the entire radial profile of the axial velocity. For a fully self-similar round jet, the velocity profile should have a functional dependence on the non-dimensional radial-over-axial distance coordinate $\eta = r/(x - x_0)$ such that $f(\eta) = \langle U(\eta)\rangle/U_0$ (Pope 2010). The radial profile of the axial velocity data collapses onto a single curve in figure 2(d), corresponding to the error function analytical solution, as found in the literature (Panchapakesan & Lumley 1993):

$$\frac{\langle U\rangle}{U_0} = \exp(-C\eta^2). \tag{3.5}$$

Figure 2(d) indicates that for $Re_g = [49200 - 130000]$ and $x/d_g = [9 - 45]$ the radial profiles of longitudinal velocity of approximately self-similar. These profiles are well approximated by equation 3.5 which is determined by C given in table 3. Similar values of C were found in (Panchapakesan & Lumley 1993).

4. Near-field break up

Two momentum ratios characteristic of different atomization regimes are pictured in figure 3. Both the low momentum ratio (fig. 3a, $M = 25.3$) and high (fig. 3b, $M = 82$) display undulations of the interface close to the nozzle, typical of the Kelvin-Helmholtz (KH) instability (Matas *et al.* 2018; Marmottant & Villermaux 2004; Lasheras & Hopfinger 2000). These instabilities may occur asymmetrically in round (Delon *et al.* 2018) and planar (Zandian *et al.* 2018) atomization and are often accompanied by the so-called flapping instability (Lozano & Barreras 2001; Delon

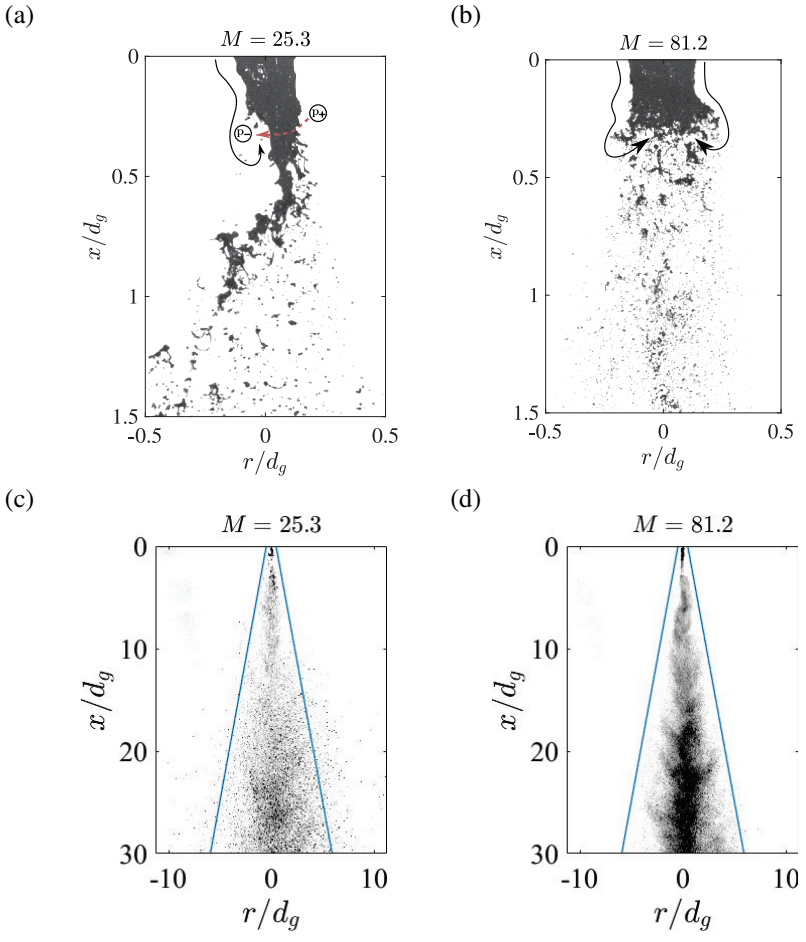

FIGURE 3. DI back-lit images in the near field. Black lines indicate gas streamlines. Relative low (high) pressure regions indicated by encircled p_- (p_+), red arrow indicates restorative force initiating flapping. (a) $M = 25.3$ (b) $M = 81.2$. DI forward scattering images in the near and far-fields for (c) $M = 25.3$ and (d) $M = 81.2$. The solid blue lines indicate the ten-percent width ($r_{0.1}/d_g$).

et al. 2018) for low liquid momentum. Flapping is apparent for the lowest momentum ratio (fig. 3a) as evidenced by strong radial excursions not observed for large momentum ratios (fig. 3b). This motion is thought to be triggered by the formation of recirculation regions in the wake of non-axisymmetric KH waves (Lozano & Barreras 2001; Zandian *et al.* 2018; Delon *et al.* 2018) leading to a local low-pressure region. Relative high-pressure regions form on the opposite side of the liquid jet and a local pressure gradient acts as a restorative force pushing the liquid jet (right to left in figure 3(a)). Experimental (Lozano & Barreras 2001; Delon *et al.* 2018) and numerical (Ling *et al.* 2019) observation of the turbulent wake on the lee side of KH waves and the subsequent liquid deformation provides evidence for this mechanism.

These radial excursions are quantified by investigating the likelihood of liquid occupying a given position in the flow field, calculating its probability of presence (P) over the entire time of study. The method is detailed in Machicoane *et al.* (2020) in the same facility presented here. Background-corrected images appear nearly binary due to the strong density interface between the gas, which appears as a 0, and the liquid as a 1. A threshold background-corrected pixel value of 0.5 is chosen to create a binary image, though this value does not significantly impact the results.

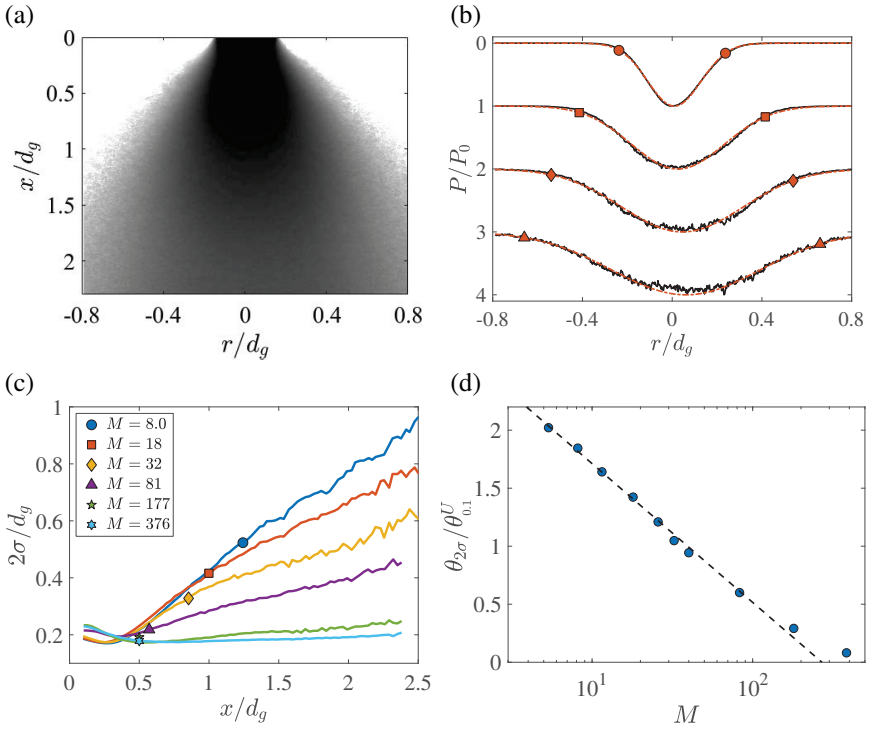

FIGURE 4. Quantification of spreading in the near field. (a) Average map giving the logarithm of the probability of liquid presence for $M = 25.3$. Black corresponds to $P = 1$ and white to $P = 0$. (b) Black lines are slices (in linear scaling) through the average map at $x/d_g = [0.5,\ 1.0,\ 1.5,\ 2.0]$ for $M = 25.3$. Plots have been shifted for clarity. Red lines are Gaussian fits where the symbols (•, ■, ♦, ▲) correspond to 2σ at each position ($x/d_g = [0.5,\ 1.0,\ 1.5,\ 2.0]$) . (c) Evolution of 2σ profiles with downstream distance for a representative sample of momentum ratios. (d) Opening angle of the spray normalized by the opening angle of the gas phase. The dashed lines correspond to the correlation: $\theta_{2\sigma} = 59.9 - 10.6 \times \log(M)$.

The arithmetic average of each pixel gives P for a statistically significant number of independent realizations. The complementary background-corrected images are presented in figure 3 for ease of viewing. In figure 4(a) the logarithm of P is plotted and values corresponding to $P = 1$ appear in black and indicate locations only occupied by liquid. Values corresponding to $P = 0$ appear in white where liquid is never present. Radial slices through this plane are plotted, normalized by the probability at the center line (P_0), in figure 4(b). Representative slices (in black) throughout the near-field were found to be well approximated by a Gaussian profile centered on $r = 0$ (in red) and are therefore fully characterized by the standard deviation σ.

The radial extent of the spray is approximated by the local value of 2σ which bounds 95.45% of the liquid presence when symmetry about the centerline is accounted for. Figure 4(c) represents the evolution of the 2σ profile in the near-field region for a few representative momentum ratios. The sudden increase in width of the profiles for $x/d_g > 0.25$ continues until the location where liquid detaches from the intact liquid core. This position, called the intact length, is marked by the symbols in figure 4(a) using the correlation in Machicoane *et al.* (2020). However, optical occlusion of the intact core prevents the exact determination of the intact length for $M = [177, 376]$ and they are estimated by the minima in the 2σ profiles. A critical value of $M \approx 50$ was identified by Lasheras & Hopfinger (2000) where the intact length is truncated by a recirculating gas cavity that creates a hollow core in the intact liquid jet (see fig. 9c in Machicoane *et al.* (2019)) and limits the progression of the intact length towards the nozzle.

The gas streamlines of this process are sketched in figure 3(b). At the highest momentum ratios ($M > 81.2$), the liquid core essentially acts as a backward facing step when streamlines separate from the truncated liquid core (sketched in fig. 3 b). Spectral content is likely broadband, with frequencies originating by the vortices shedding from the shear layer, as well as lower frequencies from the instability of the cavity itself similar to a backward-facing step (Eaton & Johnston 1980, 1982). Flapping and oscillation due to an unsteady recirculating gas cavity are separate phenomena affecting the liquid core, and are characteristic of low and high momentum ratios (respectively) with the transition occuring at $M \approx 50$.

Calculating a linear regression for $x/d_g = [1.5-2.25]$ in figure 4(c), we quantify the spreading rate ($S_{2\sigma}$) and then calculate the opening angle of the spray:

$$\theta_{2\sigma} = 2\tan^{-1}(S_{2\sigma}), \tag{4.1}$$

plotted in figure 4(d) against the spreading angle of the gas phase $\theta^U_{0.1}$. Interestingly, for $M \lesssim 40$, the dispersed liquid in the near-field has a greater spreading angle than the gas phase, while for $M \gtrsim 40$, the spray has a lower spreading angle than the gas phase. We note that the critical momentum ratio $M \approx 40$ is indicative of the overall trend and is close to the critical value of $M = 50$ given by Lasheras & Hopfinger (2000).

Caution should be taken when interpreting the highest momentum ratios ($M > 176.6$). We expect that the lateral extent of the average profiles to be slightly underestimated due to the coarse image resolution (29μm/pixel) with respect to the smallest droplets (arithmetic average $d_{10} <$ 10 μm) and to image blur related to the exposure time of the camera (0.3 μs) . The opening angle $\theta_{2\sigma}$ would be expected to deviate more strongly from the dashed line if all droplets were resolved and we interpret these angles as lower bounds that account for larger, mass-carrying droplets.

The amplification or suppression of strong radial excursions by the intact liquid core is expected to play a strong role in determining the mixing of the droplet phase in the far-field of the jet. It can be seen that large droplets are ejected from the jet's core at the nozzle (fig. 3a) and are found beyond the ten-percent width (blue lines) in figure 3(c) for $M = 25.3$. At higher momentum ratios ($M = 81.2$), droplets are more confined toward the centerline (fig. 3d). In the next section, we investigate the dispersion of liquid mass throughout the jet *via* PDI measurements.

5. Spray structure in the far-field

The interactions of the gas and liquid phases at the intact liquid-jet interface explain the narrowing of the spray in the near-field. Subsequent droplet advection into the far-field ($7 < x/d_g < 45$) is described by the evolution of the volume fraction (VF: ϕ) and volume-flux density (VFD: $\dot{g}$) and are discussed in this section.

5.1. *Volume-flux density and volume-fraction definitions*

The VFD is calculated for each diameter class, i, containing a total number N_i of droplets:

$$\dot{\mathcal{G}}(d_i) = \frac{\pi}{6T_s\mathcal{A}_i}\sum_{j=1}^{N_i} d_{j,i}^3, \tag{5.1}$$

where T_s is the total sample time, $\mathcal{A}_i$ is the probe cross-section (eq. 2.1) of the j^{th} droplet of the i^{th} size class with diameter $d_{j,i}$. We can calculate the VF assuming a single droplet occupies the probe volume at a time for the i droplet class:

$$\Phi(d_i) = \frac{\pi}{6}\frac{\tilde{t}_i}{T_s\mathcal{V}_i}\sum_{j=1}^{N_i} d_{j,i}^3, \tag{5.2}$$

where $\tilde{t}_i$ is the residence time of a droplet in the size-class probe volume $\mathcal{V}_i$ (eq. 2.2). Both equation 5.1 and equation 5.2 are defined over a given binned droplet size class. Between 15 and 21 binned size classes (index i) are used, with fewer bins used for higher momentum ratios M. A more general quantity obtained by integrating over all D droplet size classes,

$$\dot{g} = \sum_{i=1}^{D} \dot{\mathcal{G}}(d_i), \tag{5.3}$$

is the volume flux density for all droplet size classes and,

$$\phi = \sum_{i=1}^{D} \Phi(d_i), \tag{5.4}$$

the volume fraction for all droplet size classes. These quantities are understood to be time averages of instantaneous values of volume-flux density and volume fraction.

It is important to note that not every drop passing through the PDI probe volume is captured. Due to the gaussian nature of the laser beam, smaller droplets scatter less light than large droplets at the beam's edge. We correct for the bias that arises in the flux and volume fraction measurements by introducing size-dependent probe areas (eq. 2.1) and volumes (eq. 2.2). Other biases such as multiple droplets and non-spherical droplets in the probe volume as well as multi-mode scattering are corrected for (Bachalo 1994) but lead to a sub-sampling of the droplet population. When the volume flux density (eq. 5.4) is integrated over the spray cross-section for different downstream locations and the total volume flux is measured, values are found around [12.5-25]% of the nominal value at the nozzle for each momentum ratio. Similarly, the droplet-size distributions averaged over the spray cross-section to give an arithmetic mean diameter, d_{10}, vary by at most 8% of the average value over all downstream locations. Consistency in the area-averaged volume flux and diameter measurements in the far-field indicate that despite the fact that the PDI subsamples the droplet population in the spray, these measurements are unlikely to introduce a bias in the droplet populations.

5.2. *Volume-flux density and volume fraction profiles*

The VF and VFD, normalized by their maximum values for different momentum ratios, are plotted against the self-similar coordinate $\eta = r/(x - x_0^{\langle U \rangle})$ in figure 5 for different distances downstream of the nozzle. Increasing the gas flow rate (increasing M) narrows both the volume flux density (fig. 5a) and the volume fraction (fig. 5b) profiles as observed with similar co-axial atomizers (Engelbert *et al.* 1995; Hardalupas & Whitelaw 1993, 1994). An important difference between the VFD and VF is that the former is narrower than the latter over the range of momentum ratios investigated, in line with earlier observations (Hardalupas *et al.* 1989) in a particle-laden jet. While the VFD is always narrower than the average velocity profile (fig. 5a), the VF profile straddles the velocity profile (fig. 5b) depending on momentum ratio. For a critical momentum ratio, $M \approx 56$, the average concentration profile roughly follows the average velocity profile.

For each momentum ratio plotted in figure 5, profiles from different downstream locations collapse onto a single curve, when the self similar coordinate η is used. We denote this self-similar region the "far-field", occurring roughly from $7 < x/d_g < 45$, in agreement with the particle-laden jet observations in Picano *et al.* (2010). Although this parameter accounts for the self-similarity of the profiles with downstream distance, it doesn't account for variation in profile

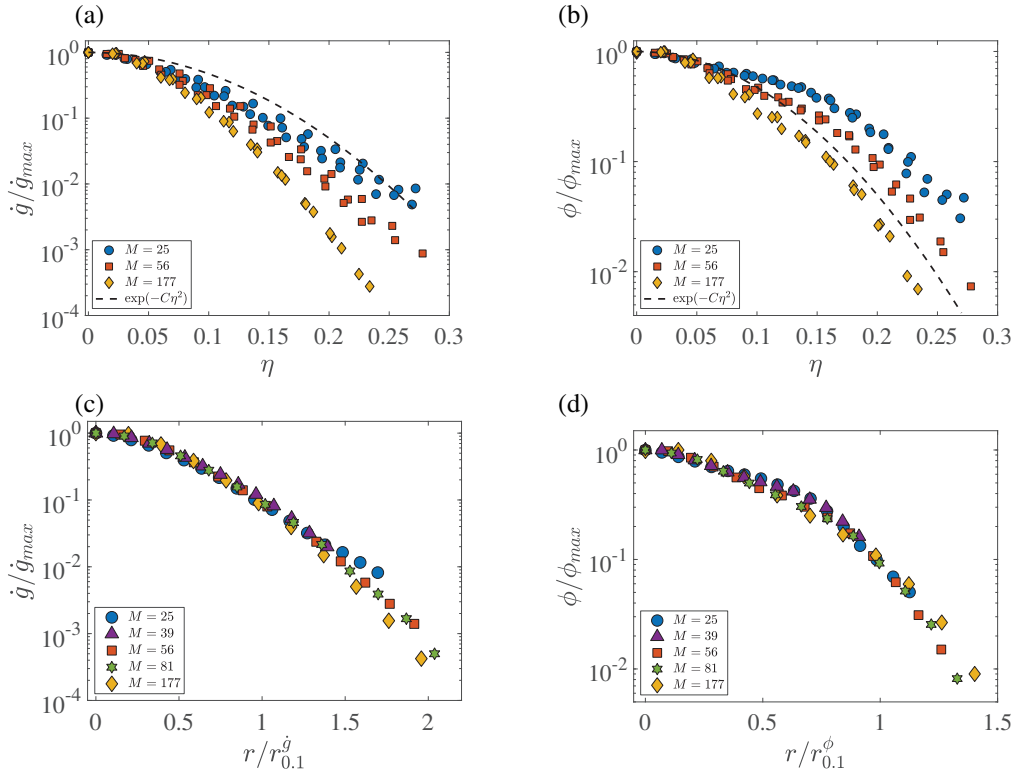

FIGURE 5. Comparison of volume flux density (VFD: $\dot{g}$) and volume fraction (VF: ϕ). (a-b) VFD and VF normalized by value at centerline plotted against the self-similar coordinate $\eta = r/(x - x_0)$ for $x/d_g = [9,\ 12,\ 18,\ 24]$. The momentum in the liquid phase is constant while varying gas-phase momentum $M = [25,\ 56,\ 177]$.(c-d) VF and VFD profiles are normalized by the ten-percent width coordinate defined in equation 5.5 at $x/d_g = [18]$.

shape as the momentum ratio is varied. Using the 10-percent width defined as:

$$\dot{g}\left(r^{\dot{g}}_{0.1}\right) = 0.1\dot{g}_{max}, \tag{5.5}$$

$$\phi\left(r^{\phi}_{0.1}\right) = 0.1\phi_{max}, \tag{5.6}$$

$$\langle U\rangle\left(r^{U}_{0.1}\right) = 0.1\langle U\rangle_{max}, \tag{5.7}$$

we normalize the VF and VFD in figure 5(c-d). We focus on the the 10-percent width because it was found to be more sensitive to momentum-ratio-dependent changes in the tails of the curves (*e.g.* fig. 5a-b) than the more common half-width metric. The normalized VF and VFD profiles display a satisfactory collapse at $x/d_g = 18$ in figure 5(c-d). This collapse indicates that the momentum-ratio-dependent physics governing the shape of the VF and VFD profile is captured by an appropriate choice of a self-similar variable in agreement with observations in the literature (Picano *et al.* 2010; Lau & Nathan 2016).

For all M, the 10-percent width (both VF and VFD, fig. 5 a-b) evolve linearly in the far-field of the jet. In general, as the momentum ratio increases, the width of the spray (either by VFD or VF) is narrower, similar to Engelbert *et al.* (1995). Near the critical momentum ratio, $M \approx 56$, we find that $r^{\phi}_{0.1} \approx r^{U}_{0.1}$. For $M > 56$, we find that $r^{\phi}_{0.1} < r^{U}_{0.1}$ and for $M < 56$ that $r^{\phi}_{0.1} > r^{U}_{0.1}$, in accordance with the self-similar VFD profiles in figure 5(a-d), $r^{\phi}_{0.1} > r^{\dot{g}}_{0.1}$ for all x/d_g.

Both the VFD and VF are governed by the spreading rate in the far-field of the turbulent jet

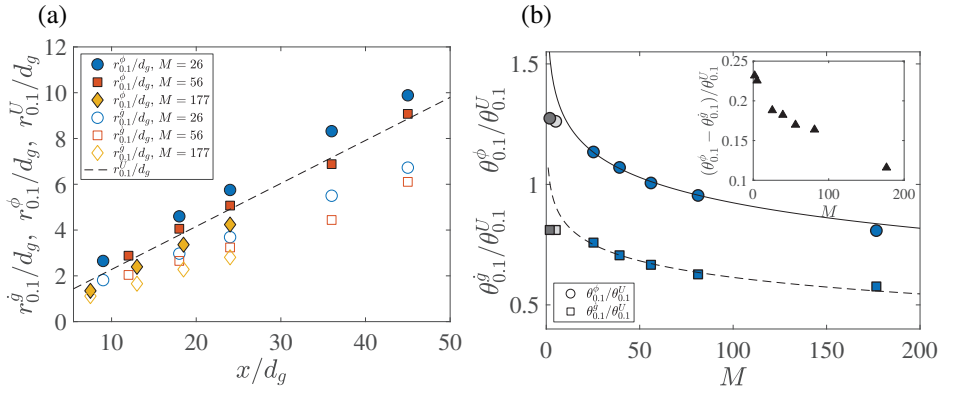

FIGURE 6. Evolution of VFD and VF profiles. (a) Normalized 10-percent width compared against the self-similar jet solution (dashed line) for $M = [25,\ 56,\ 177]$. (b) Opening angles calculated of the VF/VFD profiles normalized by the opening angle (eq. 5.11) of the gas-phase. Points in blue correspond to $Re_L = 1050$, in light gray to $Re_L = 2900$ and $M = 5.1$, and dark gray to $Re_L = 4770$ and $M = 1.9$. Solid (dashed) line describes the logarithmic trend as $\theta^{\phi}_{0.1}/\theta^{U}_{0.1} = 1.625 - 0.153\log(M)$ ($\theta^{\dot{g}}_{0.1}/\theta^{U}_{0.1} = 1.625 - 0.153\log(M)$) (inset) Difference in opening angle of VF and VFD with respect to the opening angle of the gas.

and are defined in a similar manner to the spreading rate of the velocity profile in equation 3.3:

$$S^{\dot{g}}_{0.1} = dr^{\dot{g}}_{0.1}/dx, \tag{5.8}$$

$$S^{\phi}_{0.1} = dr^{\phi}_{0.1}/dx, \tag{5.9}$$

$$S^{U}_{0.1} = dr^{U}_{0.1}/dx. \tag{5.10}$$

We take the spreading rate to be the value of η where the 7th order polynomial interpolation of ϕ/ϕ_{max} and $\dot{g}/\dot{g}_{max}$ in figures 5(a-b) reaches 10%. Similar values are obtained from a linear fit of figure 6(a). The opening angle of the volume-flux density, volume fraction, and velocity with respect to the 10-percent width is given by:

$$\theta^{\dot{g}}_{0.1} = 2\tan^{-1}\left(S^{\dot{g}}_{0.1}\right), \tag{5.11}$$

$$\theta^{\phi}_{0.1} = 2\tan^{-1}\left(S^{\phi}_{0.1}\right), \tag{5.12}$$

$$\theta^{U}_{0.1} = 2\tan^{-1}\left(S^{U}_{0.1}\right), \tag{5.13}$$

The evolution of the opening angles of each metric with respect to the opening angle of the jet $\theta^{U}_{0.1} = 20.6°$ is plotted in figure 6(b) as a function of momentum ratio. Data for constant liquid flow rate and variable gas flow rate (blue) and constant gas flow rate and variable liquid flow rate (shades of gray) are given. For all momentum ratios, we observe that the opening angle of the VFD profiles are smaller than the VF. The opening angle decreases with increasing momentum ratio and, past $M \approx 10$, and follow a logarithmic trend. The critical momentum ratio $M \approx 56$ is observed to indicate the threshold beyond which the VF profiles spread less than the gas phase. Due to the agreement of the observations of critical behaviors in spreading rates of liquid presence and VF in both near and far field, respectively, we define an overall critical momentum ratio of $M_c = 50$.

The logarithmic dependency of $\theta^{\dot{g}}_{0.1}$ and $\theta^{\theta}_{0.1}$ will not continue to arbitrarily large M because the opening angles cannot be negative. The opening angles of the VF profiles tend toward that of the VFD (fig. 6b,inset) suggesting that an asymptotic regime where $\theta^{\dot{g}}_{0.1}/\theta^{\phi}_{0.1} \to 1$ and $\theta^{\dot{g}}_{0.1}/\theta^{U}_{0.1} < 1$ is likely. This is because radial transport of the droplet phase is sustained by the radial transport of gas momentum. Thus, for arbitrary M, the radial expansion of the VFD profile

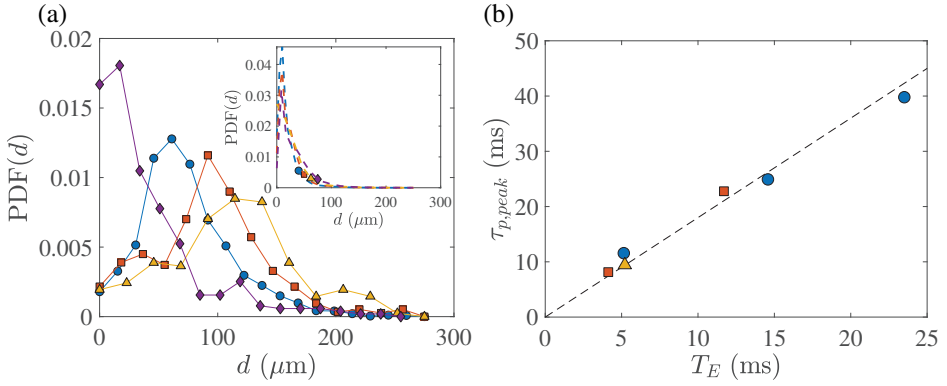

FIGURE 7. Characterization of droplet size PDFs on the spray's edge (a) PDFs for $M = 25.3$, radial position $r \sim 1.5r_{0.1}$, downstream position $x/d_g = [9, 18, 24, 36]$, ([•, ■, ▲, ◆] respectively). PDFs display a predominant mode that is characteristic of $M = [25.3,\ 39.2,\ 56.0]$ except for $x/d_g = 36$. (inset) PDFs at $r/d_g = 0$ with modes of $\mathcal{O}(10\ \mu\text{m})$. Symbols correspond to downstream position. (b) The droplet size corresponding to the mode when $r \sim 1.5r_{0.1}$, $d_{p,peak}$, is assigned the characteristic droplet timescale $\tau_{p,peak} = \rho_\ell d_{p,peak}^2/(18\nu_g\rho_g)$ and compared with the integral scale T_E (eq. 6.1).

may approach, but not exceed, the radial expansion of the gas-phase profile.

6. Droplet presence at the spray's edge

In this section, the presence of large droplets on the spray's edge is linked to their inertia with respect to the large-scale structures in the spray. This framework permits of description of the radial droplet-size profiles within the broader context of the parameter range of turbulent round jet sprays (sec. 7).

6.1. *Liquid Ligament Ejection*

In figure 3(c-d), two sprays are imaged, one where $M < M_c$ and the other with $M > M_c$. In the far field of the former, at $x/d_g \approx 24$, droplets are clearly detected beyond the edge of the gas jet ($r_{0.1}^U/d_g = 4.8$) given by the blue lines, with some even observed near $r/d_g = \pm 10$. For $M < M_c$, large droplets can be found on the jet's edge, however the finite resolution of the images and weak light scattering by small particles may obscure their presence in these images.

To confirm the dominance of large drops near the edge of the spray for $M < M_c$, probability density functions (PDFs) were calculated for $M = 25$ at four downstream locations for $r \sim 1.5r_{0.1}$ in figure 7(a). With the exception of $x/d_g = 36$, each PDF displays a peak for diameters much larger ($d > 66\ \mu$m) than the typical peak of the spray droplet-size distribution near the centerline ($d = \mathcal{O}(10\ \mu\text{m})$, fig. 7 a,inset). We refer to the droplets constituting the secondary peaks at the spray's edge as *ejections*. This peak diameter increases in size with downstream distance until $x/d_g = 36$, where it shifts back to a smaller droplet diameter. Beyond $M \approx M_c$, no peak corresponding to an ejection is observed.

This phenomenon can be explained by the interaction of ejections with the largest eddies of the turbulent jet. The role of the eddies in selectively transporting droplets was proposed by Chung & Troutt (1988) and subsequently experimental (Lazaro & Lasheras 1992*a*; Longmire & Eaton 1992) and numerical (Sbrizzai *et al.* 2004) investigation in different shear-driven flows have largely supported this hypothesis. These eddies are characterized by an Eulerian timescale:

$$T_E = 2r_{0.1}/u', \tag{6.1}$$

where u' is the longitudinal velocity fluctuations on the centerline and $2r_{0.1}$ approximates the diameter of the gas jet at a given downstream position. This length scale is chosen because the literature suggests the presence of large axisymmetric and helical structures (Dimotakis *et al.* 1983; Mungal & Hollingsworth 1989) that persist into the far field of the jet and are correlated over its width (Yoda *et al.* 1992; Tso & Hussain 1989). Similar definitions of T_E have been used (Prevost *et al.* 1996) to characterize large-scale motions over the entire jet cross-section.

The ejections for $M = [25,\ 39,\ 56]$ are used to calculate a time scale based on the characteristic diameter at the peak $d_{p,peak}$ in figure 7(a):

$$\tau_{p,peak} = \rho_\ell d_{p,peak}^2/(18\nu_g\rho_g) \tag{6.2}$$

and are plotted as a function of their local Eulerian time scale T_E in figure 7(b). The ejections collapse on a single line whose slope gives a Stokes number characteristic of the ejections:

$$St_{peak} = \tau_{p,peak}/T_E. \tag{6.3}$$

A slope of $St_{peak} = 1.9$ is measured and is of order one, strongly suggesting that large eddies are responsible for the presence of liquid ejections on the edge of the spray.

Experimental evidence in particle-laden jets (Hardalupas *et al.* 1989) and sprays (Engelbert *et al.* 1995) suggests that the initial conditions seen by a particle at injection determine a ballistic trajectory until the local Stokes number with respect to the large energy containing scales becomes of order one. In the case when $M < M_c$, the radial velocity associated with the flapping instability sends droplets on ballistic trajectories as they are ejected from the jet. Then, droplets traveling downstream for which $St < St_{peak}$ would be less probable at the spray edge because they have been re-entrained on the upstream side of the eddy where the entrainment process is strongest (Lampa & Fritsching 2013). Such an entrainment process would culminate in predominantly smaller droplets on the spray's edge, explaining the shift to smaller droplet modes between $x/d_g = [24 - 36]$ in figure 7(a).

6.2. *Ejection relaxation to the gas phase*

To determine if droplets capable of interaction with large eddies exist within the spray, we have calculated the normalized and radially-integrated VFD conditioned on droplet size. As opposed to the size-conditioned VFD at a given radial location (eq. 5.1), an integral VFD was calculated over successive annuli of the spray centered on the position of the PDI probe volume and weighted by the relative area of each annuli. The probability of finding droplets within the annulus is assumed to be statistically homogeneous. Finally, the conditioned and weighted VFD was normalized by the sum over all sizes. We call this normalized metric the Volume Flux Density Function (VFDF) and it is implied in the following section that it is a quantity integrated over a cross-section of the spray although it can also be evaluated locally (sec. 7). The VFDF relates the volume flux density (volume per unit area and unit time) carried by a droplet with diameter between d and $d + \mathrm{d}(d)$. In fact, the VFDF contains the same information as the number flux density (number per unit area and unit time), commonly referred to as the PDF, and the two are analytically related (appendix A).

Once atomization has occurred, and assuming coalescence and evaporation are negligible in the short residence times in the near to far field droplet trajectories, the VFDF remains essentially unchanged as the spray evolves downstream†. The VFDFs are presented in figure 8(a) for $M = [25.3 - 176.6]$ at $x/d_g = 24$ but other locations collapse on the same curve. Narrowing of the VFDF with increasing M is characterized by a decrease in the d_{43}^i (mass flux weighted) diameter

† Preserved values of arithmetic and volume averaged diameters was taken to be an indication of high-quality PDI measurements in section 5.1 for this reason.

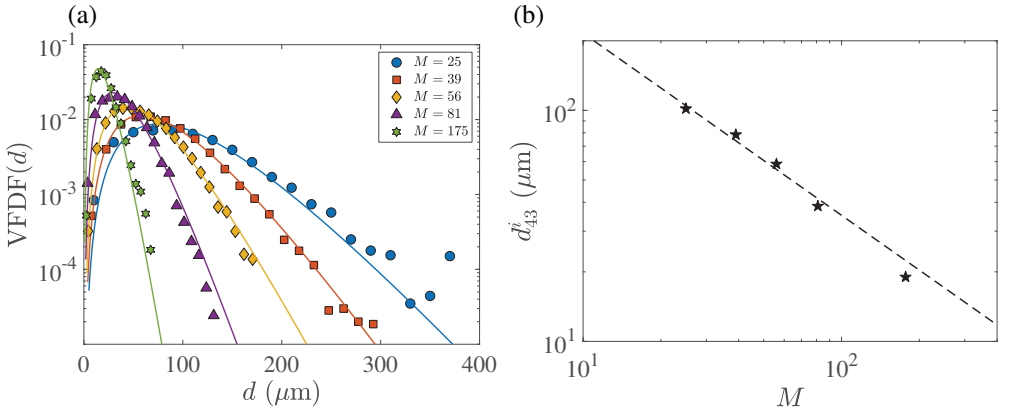

FIGURE 8. Radially integrated measurements taken at $x/d_g = 24$ characteristic of the entire spray cross-section. (a) Volume Flux Density Function (VFDF) for different momentum ratios. Solid lines correspond to equation 6.5 with $n = 3.9$. (b) First moment of the VFDF evaluated over the spray cross-section, d^i_{43}, at $x/d_g = 24$ for various M.

which is the first moment of the VFDF (eq. B 3). The superscript i indicates that the VFDF is integrated over the spray cross-section and its first moment (d^i_{43}) is a global characteristic of the spray at a given downstream location x/d_g. Absence of the superscript indicates that the VFDF is evaluated at a given downstream and radial location and its first moment (d_{43}) is a local characteristic of the spray. The d^i_{43} follow a power law: $d^i_{43} \propto M^{-0.79}$ and are plotted in figure 8(b).

Interestingly, the VFDF can be described by a single parameter gamma function:

$$\Gamma(n, x = d/d^i_{43}) = \frac{n^n}{\Gamma(n)} x^{n-1} \exp(-nx). \tag{6.4}$$

which gives the following approximation:

$$\mathrm{VFDF}(d) = \frac{1}{d^i_{43}} \Gamma(n, d/d^i_{43}), \tag{6.5}$$

as observed by solid lines in figure 8(a). The VFDFs can be collapsed onto a single master curve given by equation 6.5 using $n = 3.9$ and d^i_{43} in figure 8(b). This implies that for both $M < M_c$ and $M > M_c$, sprays are governed by the same atomization mechanism, which has been attributed to the dynamics of ligaments formed by the coaxial gas jet (Marmottant & Villermaux 2004; Villermaux *et al.* 2004).

The mass flux-weighted average diameter d^i_{43} is indicative of the characteristic droplet carrying the overall mass flux in the spray. The characteristic time-scale based on this droplet size class is:

$$\tau_{43} = \rho_\ell (d^i_{43})^2 / (\rho_g 18 \nu_g). \tag{6.6}$$

A comparison of T_E and τ_{43} at $x/d_g = 18$ for several momentum ratios is plotted in figure 9(a). If a droplet is resonant with the large eddies, then $\tau_{43} \sim T_E$. If $\tau_{43} > T_E$, there must be some droplets for which $\tau_{43} \sim T_E$ and ejections at the spray's edge are likely. However, if $\tau_{43} < T_E$, it is assumed that there are no droplets in the spray resonant with the large eddies and no, or few, ejections exist.

Evolution in droplet interactions with the large scale eddies at a given x/d_g is captured by a global Stokes number:

$$St_{43} = \tau_{43}/T_E. \tag{6.7}$$

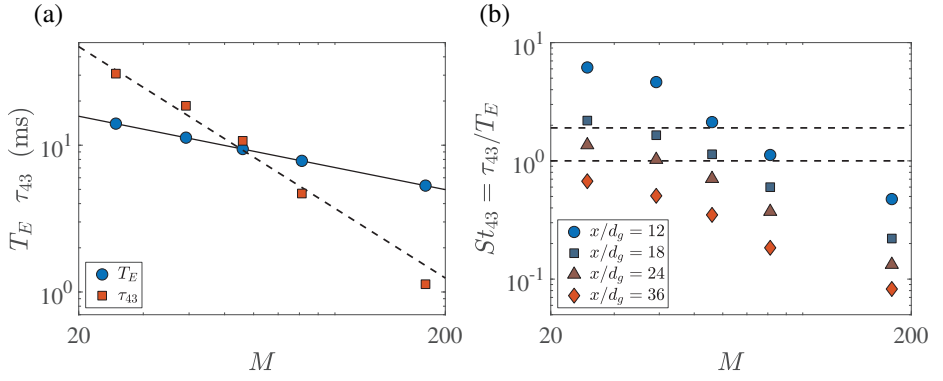

FIGURE 9. Evolution of area-averaged droplet time scale with M and x/d_g. (a) The droplet response time τ_{43} based on the d^i_{43} diameter and the large-eddy time scales T_E vary as a function of M. Dashed line is $\tau_{43} \approx 5.3 \times 10^3 M^{-1.58}$ and the solid line is $T_E \approx 70.4 \times M^{-0.50}$. (b) Evolution of the Stokes number for the peak probability droplet, as a function of the momentum ratio. Different symbols represent different downstream locations. Values above $St_{43} = 1.9$ represent combinations where ejections are possible, values below $St_{43} = 1.0$ are combinations where ejections are unlikely.

For a given momentum ratio M in figure 9(b), St_{43} decreases with downstream location because τ_{43} is constant and $T_E \propto (x/d_g)^2$. The range $St_{43} > St_{peak}$ ($St_{peak} = 1.9$) corresponds to strongly inertial droplets and high ejection probability on the spray edge. The area bounded by dashed lines, $1 < St_{43} < St_{peak}$, corresponds to a transitional regime where ejections become less probable on the spray edges. Below the solid line, $St_{43} < 1$, droplets are weakly inertial with respect to the large eddies and ejection presence on the spray edges is unlikely. These observations are consistent with the momentum ratio and location where ejections were observed in figure 7.

7. Spray Regimes

While the VFDF can be evaluated over the entire spray cross-section (sec. 6.2), it can also be evaluated locally for a given downstream location (x/d_g) and radial location normalized by jet velocity ten-percent width ($r/r_{0.1}$). Profiles of first moment of the locally evaluated VFDF, or the mass-flux weighted (d_{43}) diameter, are investigated and used to characterize spray regimes that broadly fall into momentum ratio ranges: $M < M_c$,$M \approx M_c$, and $M > M_c$. To highlight their relationship with the large scale flow features, d_{43} profiles are normalized by a fictive droplet that would be resonant with the local large scale eddy,

$$\tilde{d} = (T_E 18 \nu_g \rho_g / \rho_\ell)^{1/2}. \tag{7.1}$$

This normalization masks an important aspect of the d_{43} profile evolution with downstream location. For all M, the value of d_{43} slightly increases on the centerline as the spray evolves downstream. This is a consequence of the large droplets on the centerline dispersing slower than smaller ones and therefore have a stronger statistical contribution on the centerline as the spray evolves. We note that, by definition, $(d_{43}/\tilde{d})^2$ is the local equivalent to the global Stokes number (St_{43}) defined in equation 6.7.

7.1. $M < M_c$

For the momentum ratios below M_c, the d_{43} profiles retain a "∪" shape where the smallest droplets are found near the centerline and the largest near the edge (fig. 10a-c). Within this range of M, slight differences are observed between $5.1 < M < M_c$ (figure 10 b-c) and $M < 5.1$ (figure 10 a).

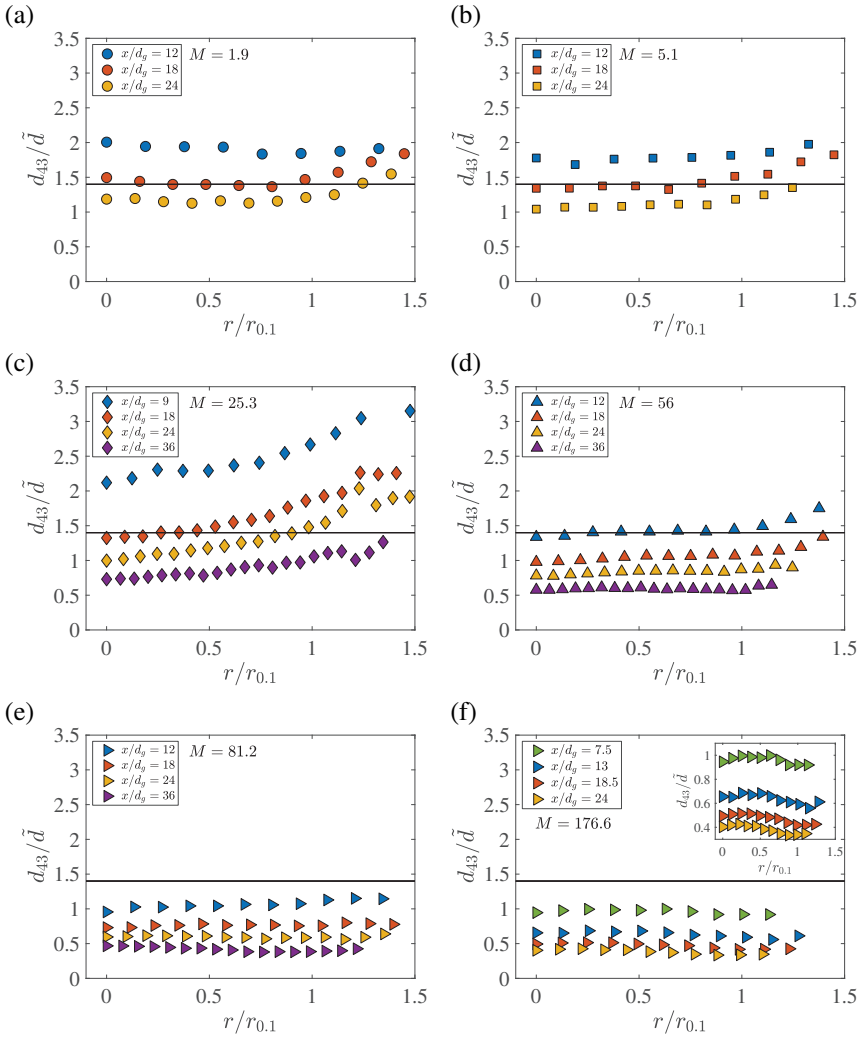

FIGURE 10. Evolution of $d_{43}/\tilde{d}$ profiles where $\tilde{d} = (T_E 18 \nu_g \rho_g/\rho_\ell)^{1/2}$ corresponds to a droplet with a characteristic time scale equal to the local Eulerian time scale T_E. Radial position is normalized by the 10% width of the gas jet as an estimate of its radius. Solid lines correspond to $(St)^{1/2} = (1.9)^{1/2} = 1.4$, the Stokes number corresponding to ejections. (a) $M = 1.9$ (b) $M = 5.1$ (c) $M = 25.3$, (d) $M = 56$, (e) $M = 81.2$, (f) $M = 176.6$ (f,inset) $M = 176.6$, reduced ordinate range emphasizing central maximum.

When $M < 5.1$ there is a non-monotonic increase in d_{43} from the centerline to the edge. There appears to be a local peak in d_{43} near the centerline which falls off until $r \sim r_{0.1}$ and the droplet diameter increases again beyond the edge of the jet, where a maxima occurs. Similar profiles were observed by Engelbert *et al.* (1995) and were attributed to delayed atomization characteristic of low momentum ratios. When break-up of the liquid core eventually occurs, it takes place further downstream in an environment with weaker shear. Large detached liquid ligaments form, which are subsequently atomized inefficiently, leading to large droplets on the centerline. Smaller droplets towards the edge are a result of their faster response to the jet turbulence. However, droplets even larger than those on centerline are found near the edge. These are likely the result of a flapping mechanism similar to the one established for larger M sprays.

For $5.1 < M < M_c$, there is a monotonic increase in d_{43} towards the edge of the spray (fig. 10

c). As suggested by Hardalupas *et al.* (1989); Engelbert *et al.* (1995), initial injection conditions lead to ballistic trajectories which persist until the droplets reach resonance with large eddies, typically for $d_{43}/\tilde{d} < (St_{peak})^{1/2}$. From figure 10(b-c) flattening in the profiles occurs when the droplets on the edge of the spray resides between $1 < d_{43}/\tilde{d} < 1.4$ similar to the range of droplet ejections that were hypothesized to interact with large scale eddies in figure 9(b).

7.2. $M \approx M_c$

Close to $M = M_c$, a confluence of factors affects the shape of the droplet diameter profiles. The liquid presence probability profiles (fig. 4d) approach values determined by the gas-phase velocity profile, ($\theta_{2\sigma} \approx \theta^U_{0.1}$) which is thought to be due to suppressed flapping as M approaches M_c. As a consequence, there are fewer large droplets on the spray edge and the VF profile in the far-field (fig. 6b) tends toward the gas-phase velocity profile ($\theta^\phi_{0.1} \approx \theta^U_{0.1}$). In figure 10(d), the diameter profile for $M = 56$ is plotted and only at $x/d_g = 12$ does the diameter profile both present the signature of ejections with a prominent central minima. For $x/d_g > 12$, the integrated Stokes number is subcritical ($St_{43} < St_{peak}$), and nearly all of the radial values fall below the ejection threshold $d_{43}/\tilde{d} = (1.9)^{1/2}$. As the droplets continue downstream the profiles begin to flatten which is indicative of droplets relaxing to the gas phase ($St_{43} < 1$) .

7.3. $M \gg M_c$

The highest momentum ratio regime is characterized by a d_{43} profile with a central maximum and minima on the edges (figure 10f). As opposed to the $M < M_c$ regime, the flapping phenomenon does not significantly contribute to the dynamics of atomization nor does it impart initial radial momentum onto the droplets. In this regime, enhanced radial transport would be possible if droplets were resonant with the large eddies. However, the timescale of the droplets produced by atomization decreases with increasing M ($\tau_{43} \propto M^{-1.58}$) at a faster rate than eddy time scales decreases ($T_E \propto M^{-0.5}$) with increasing M (increasing Re_g). This results in Stokes numbers for the droplet cloud well below unity. Due to the recirculating gas cavity present at $M \gg M_c$, larger droplets are confined to the centerline. The smallest droplets can follow the radial expansion of the gas phase closely. Thus, they are found more frequently near the edge of the jet, explaining the marked central maximum of d_{43} and the minima on the edges.

7.4. *Spray regime diagram ($We - Re_\ell$)*

The data has been presented as a function of $M = \rho_g u_g^2/(\rho_\ell u_\ell^2)$ either by experimentally varying u_g or u_ℓ, independently. However, in section 7.3 it was seen that a convex ("∩") profile with a central maximum could be observed both for low ($M = 1.9$, fig. 10a) and high momentum ratios ($M = [81.2, 176.6]$, fig. 10e-f). Instead, the $We - Re_\ell$ phase-space is introduced to account for gas and liquid phase momentum separately in the wider context of experimentally observed sprays.

PDI data from the literature presenting radial profiles of droplet size was surveyed (table 4). Results for the Sauter mean diameter (d_{32}) we found, but not for mass flux-weighted diameter (d_{43}). From the present data, the evolution of the d_{43} is found have be less extreme differences between minima and maxima but, in general, the evolution described in section 7.1-7.3 for d_{43} is similar for d_{32}. Since the profiles evolve downstream, the data displayed in the phase-space is restricted to $x/d_g < 13$.

The phase-space diagram (fig. 11) is divided into five regimes, color-coded, based on the observed droplet diameter radial profile. Note that the solid symbols correspond to the PDI data in this paper. Regime I (red) corresponds to "∪"-shaped profiles. Regime II (yellow) corresponds to flat profiles. Regime III (green), IV (blue), and V (grey) correspond to "∩"-shaped profiles.

Author	M	We	m	Re_ℓ	Re_g	x/d_g	Diameter	Symbol
-	-	-	-	-	$\times 10^3$	-	-	-
Eroglu & Chigier (1991)	1.0-13.7	29-200	0.07-0.25	1097-4370	36.9-90.	0.7-1.1	d_{32}	∘
Hardalupas & Whitelaw (1993)	0.7-0.8	730-1174	0.09-0.12	9020-17480	126-143	13.5	d_{32}	□
Hardalupas & Whitelaw (1994)	0.2-0.7	231-256	0.09-0.12	8280-17500	58.700	9-13	d_{32}	□
Engelbert *et al.* (1995)	1.2	450	0.65	8280	111.6	5-10	d_{32}	△
Zaller & Klem (1991)	0.8-72	372-3264	0.58-2.70	2570-7041	50.0-108	9	d_{32}	⋄
Zaller & Klem (1995)	1.3-2427	494-2660	0.18-2.12	451-8120	55.600-92.7	9	d_{32}	☆
Present	1.9-176.6	190-1342	0.10-0.93	1167-5305	49.200-130	7.5-13.5	d_{43}	◀

TABLE 4. Experimental parameters from the literature, used in figure 11. Momentum ratio: $M = \rho_g U_g^2/(\rho_\ell U_\ell^2)$. Weber number: $We = \rho_g(U_g - U_\ell)^2 d_\ell/\sigma$. Mass ratio: $m = \rho_\ell A_\ell U_\ell/(\rho_g A_g U)$. Liquid phase Reynolds number: $Re_\ell = U_\ell d_\ell/\nu_\ell$. Gas phase Reynolds number: $Re_g = U_g d_g/\nu_g$. Distance from nozzle where profile was measured: x/d_g. Diameter classes correspond to the Sauter Mean Diameter d_{32} and mass flux averaged diameter d_{43}.

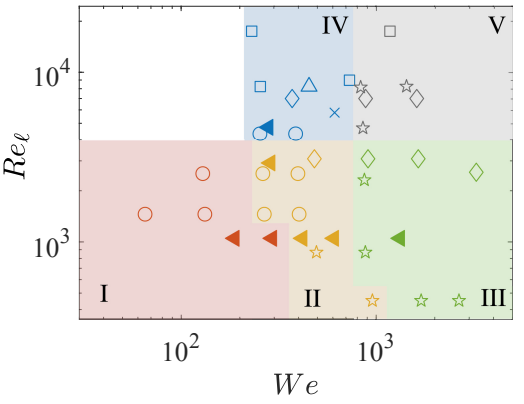

FIGURE 11. Phase space diagram ($We - Re_\ell$) indicating the shape of the radial droplet profiles for the present experiments and those found in the literature, symbols are the same as in table 4, solid symbols are the present experiments. All of the points shown correspond to measurements within $x/d_g \leq 13$ and correspond to d_{32} measurements except the present experiments (d_{43}). Colors are an indication of regime. Regime I (red) corresponds to "∪"-shaped profiles. Regime II (yellow) corresponds to flat profiles. Regime III (green), IV (blue), and V (grey) correspond to "∩"-shaped profiles. The white area is typically inaccessible to PDI measurements due to the inability of the spray to create spherical droplets in this regime.

The white area is typically inaccessible to PDI measurements due to the inability of the spray to create spherical droplets in this regime.

For $Re_\ell \lesssim 4000$ and $50 < We < 300$, the profiles fall in regime I where flapping is dominant and gives rise to other morphologies such as "ladle" Eroglu & Chigier (1991) structures (fig. 3 a,c) which launch drops beyond the gas jet creating "∪" shaped profiles. Increasing the momentum in the gas phase for $Re_\ell \lesssim 4000$ and $We \gtrsim 300$ reduces the role of the flapping instability, marking the transition from regime I to II. This transition corresponds to $M = M_c$ for our data set and a flattening of the mass flux-weighted diameter profile (fig. 10 d). If the momentum in the gas phase is increased beyond $We \sim 800$ (and $Re_\ell \lesssim 4000$), a transition between flat and "∩"-shaped profiles occurs (II to III). This regime is characterized by the emergence of a recirculating gas cavity just downstream of the liquid core.

The present data ($M < 5.1$, fig. 10a-b) help confirm the transition from regime II to IV that occurs for $200 < We < 800$ and $Re_\ell \approx 4000$. In regime IV there are large droplets near the spray edges and also on the centerline giving a "W"-shape profiles close to the transition at $Re_\ell \approx 4000$ (fig. 10a). Further into regime IV, the gas phase lacks sufficient momentum to initiate the flapping instability and the instability transitions to the "dilational waves" observed by Engelbert *et al.* (1995). These waves are sufficiently long lived for successive vortices to establish recirculation regions in the wake of the KH wave. In Zandian *et al.* (2018), vortex stretching leads to the formation of hairpin vortices in the wake region that deform these recirculating vortices which in turn deform the liquid core. This cascade gives rise to the droplets constituting "∩"-shaped profiles.

Interestingly, these profiles in regime IV ($Re_\ell \gtrsim 8000$), resemble profiles in regime III which are also "∩"-shaped and also do not exhibit flapping due to the recirculating gas cavity. While at lower We, surface tension resists the formation of droplets, in the high We regime the hairpin vortices described above are able to perforate the ligaments forming smaller droplets as described by Zandian *et al.* (2018). This mechanism helps to understand the difference in droplet sizes between regime III and IV despite similarities in the profile shape.

Regime V is not explored in this paper and deserves comment. The boundary between regime III and V is difficult to delimit as both display "∩"-shaped profile. Increasing the liquid momentum, and with it the liquid-gass mass ratio, in the spray when the gas momentum is high

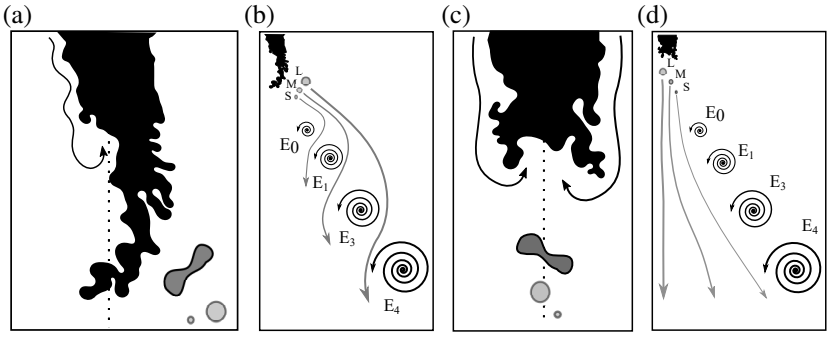

FIGURE 12. Sketch of the break-up and dispersion processes. Flow separation at the interface causes recirculation in both (a) $M < M_c$ and (c) $M > M_c$ cases. Large (L), medium (M), and small (S) droplets interact differently with a series of eddies ($E_0,\ E_1,\ E_2,\ E_3$) when $M < M_c$ and $M > M_c$. (a-b) $M < M_c$. (c-d) $M > M_c$

($We > 800$) results in increased transfer of momentum from gas to the liquid phase as more liquid is required to accelerate to the gas-phase's velocity. This may change the nature of atomization that occurs after liquid separates from the intact core, known as secondary atomization (SA). Lasheras *et al.* (1998); Lasheras & Hopfinger (2000) identify two mechanisms of SA-driven break up: mean shear and turbulence induced. The former occurs when a strong enough relative velocity occurs between the droplet and the gas while the latter is due to destabilizing turbulent fluctuations occuring over the droplet's surface. As more gas momentum is transferred to the accelerate the liquid phase, velocity fluctuations are dampened (Engelbert *et al.* 1995; Modarress *et al.* 1984) resulting in increasingly weak turbulent SA. This is thought to be the mechanism governing the spray transitions from regime III to V. However, the precise role of turbulent and shear SA in regime III and V deserves further research.

8. Discussion and conclusions

The presence of "∪", flat, and "∩"-shaped profiles is thought to be a consequence of the ability of the spray to progressively entrain *ejections* by large scale eddies on the spray's edge. Figure 12 provides a conceptual sketch of the break-up and dispersion processes discussed in this paper.

Within the inner shear layer which forms between the liquid and gas jets at $M < M_c$ (fig. 12 a), interfacial instabilities grow until the gas flow separates and recirculates behind the perturbation. Separation causes a pressure gradient to establish across the liquid jet (dark black) causing it to flap and produce liquid ligaments (medium gray) which form smaller stable droplets (light gray) that may be found far from the jet centerline. The dispersal of a "small" (time scale: τ_{ps}), "medium" (τ_{pm}), and "large" (τ_{pl}) droplet in the far field is depicted in figure 12(b).

The droplets travel with ballistic trajectories until they encounter eddies in the far-field with the same sense of rotation as those originating in the outer shear layer formed between the co-axial gas flow and stagnant ambient fluid in the near field. Droplet trajectories are eventually perturbed by these far-field eddies E with time scales $[T_{E0}, T_{E1}, T_{E2}, T_{E3}]$ based on equation 6.1. At E_0, all droplets are inertial such that $T_{E0} < \tau_{ps} < \tau_{pm} < \tau_{pl}$ and they overshoot the eddy. By virtue of its imminent entrainment, τ_{ps} is at the threshold for ejections at E_0 and $\tau_{ps}/T_{E0} \approx 1.9$ determined in section 6.1. At E_1, the smallest droplets are resonant with the eddies ($\tau_{ps} \approx T_{E1}$) and are entrained on the upstream side of the eddies. Meanwhile, $T_{E1} < \tau_{pm} < \tau_{pl}$ and the medium and large droplets continue ballistically with the new ejection threshold $\tau_{pm}/T_{E1} \approx 1.9$. The entrainment process continues at E_2, where the $\tau_{pm} \approx T_{E2}$ and $\tau_{pl}/T_{E2} \approx 1.9$. Finally, the large droplets are entrained at E_3 when $\tau_{pl} \approx T_{E3}$ leaving none of the initial ejections near the edge

of the jet. The progressive entrainment of large droplets from the spray's edge is thought to be responsible for the flattening of the droplet-size profiles when $M < M_c$.

Due to the increased momentum in the gas phase, the inner shear layer establishes a recirculating gas cavity just downstream of the liquid jet (black shading) for $M > M_c$ (fig. 12 c). The presence of this shear layer is responsible for liquid ligaments (medium gray) that are stripped from the intact liquid jet much earlier than for the $M < M_c$ case. These ligaments eventually break down into droplets (light gray), which are concentrated in the vicinity the gas jet's centerline (dotted line). The large droplets are essentially ballistic and deviate very little from the centerline while the smallest droplets are more sensitive to large eddies and can be transported radially (fig. 12d). In this regime, $St_{43} \lesssim 1$ and as the droplets travel downstream they become less inertial and begin to follow the gas phase, causing them to be swept into the downstream side of the outer shear-layer eddies. This creates the "branching" pattern at the sprays edge on figure 3(d) as the droplets are transported toward the spray's exterior. Similar observations have been made in droplet-laden two-dimensional shear layers (Lazaro & Lasheras 1992*a*), as well as in co-axial atomizers (Lampa & Fritsching 2013). Despite the droplets interacting with large scale structures at $M > M_c$, the spray is significantly narrower due in large part to the liquid core's inability to shed droplets far from the centerline, as is the case for $M < M_c$.

The ratio of mass flux-weighted diameter (d^i_{43}) to the diameter of the droplet that would be resonant with a local large eddy ($\tilde{d}$) allows an *a priori* estimation of the mass-flux weighted droplet-size profiles that develop in the dispersion regimes above. Profiles with a predominant central minimum and edge minima ($d^i_{43}/\tilde{d} > 1.4$, $M < M_c$) arise when ejections are found at the spray's edge due to flapping. For momentum ratios close to the critical value ($M \approx M_c$), mostly flat profiles arise for $0.6 \lesssim d^i_{43}/\tilde{d} \lesssim 1.4$. For $M > M_c$, suppressed flapping and the absence of ejections result in profiles with a predominant central maximum and edge minima arise with $d^i_{43}/\tilde{d} \lesssim 0.6$.

This paper experimentally investigated the dispersion regimes in the far-field of a spray produced by a co-axial two-fluid atomizer. It was found that the presence of known atomization mechanisms in the near-nozzle region strongly impacts the dispersion of droplets in the far field. A critical momentum ratio of $M_c = 50$ separates a regime with significant liquid presence beyond the edge of the gas jet ($M < M_c$) from a regime with most of the liquid confined within the gas-jet boundaries ($M > M_c$). To the best of the authors' knowledge, and despite the maturity of the spray physics field, no explanation for the rich variety in droplet-size profiles found in the literature has yet been given. We have linked the above regimes to three classes of droplet-size profile shapes and established a framework for predicting them based on relevant spray parameters. Amongst these, the critical Stokes number $St = \tau_p/T_E = 1.9$ indicates droplets that are susceptible to dispersing beyond the nominal extent of the gas phase. The ability to predict evolving spray shape with different gas/liquid parameters may prove useful in various spray control applications where a dynamically varying spray with known characteristics may be required (Osuna-Orozco *et al.* 2019, 2020).

Appendix A. Relationship between PDF and VFDF

Intuition suggests that the PDF and VFDF are related. The former expresses the probability that a certain *number* of droplets is observed, the latter that a *volume* is observed. Below, we show that that the PDF is mathematically equivalent to the normalized number-flux density function NFDF. We prefer to use the number density function (NFDF) than the PDF as it specifies *how* the measurements we made (*i.e.* per unit area per unit time). We show that the NFDF and VFDF are related analytically.

The probe cross-sectional area can be written $\mathcal{A}_i = L\ell = L\overline{\ell}(1+b_i)$ where $b_i = (1+(\ell_i - \overline{\ell})/\overline{\ell})$

relative to the i^{th} droplet diameter class with probe length ℓ_i given an average probe length $\overline{\ell}$. The volume flux density (VFD) per size class is given by,

$$\dot{\mathcal{G}}(d_i) = \frac{\pi}{6T_s\overline{\mathcal{A}}(1+b_i)} \sum_{j=1}^{N_i} d_{ij}^3, \tag{A 1}$$

where $\overline{\mathcal{A}} = L\overline{\ell}$. Note that the factor $(1 + b_i)$ acts as a multiplicative constant related to the bias towards large droplets in particle counting systems. It corrects for an overestimation of large droplets as the path length ℓ for small droplets is smaller than for large droplets. The VFD summed over D total size classes is:

$$\dot{g} = \sum_{i=1}^{D} \dot{\mathcal{G}}(d_i). \tag{A 2}$$

The unbiased volume-averaged diameter is calculated as,

$$d_{30} = \left(\Big(\sum_{i}^{D} (1+b_i)^{-1} \sum_{j}^{N_i} d_{ij}^3 \Big) \Big(\sum_{i}^{D} (1+b_i)^{-1} \sum_{j}^{N_i} 1 \Big)^{-1} \right)^{1/3}. \tag{A 3}$$

Normalization of the VFD gives the volume flux density function (VFDF),

$$\mathrm{VFDF}(d_i) = \frac{\dot{\mathcal{G}}(d_i)/\mathrm{d}d}{\dot{g}} = \frac{1}{\mathrm{d}d} \sum_{j=1}^{N_i} \frac{d_{ij}^3}{(1+b_i)} \Big(\sum_{i=1}^{D} \sum_{j=1}^{N_i} \frac{d_{ij}^3}{(1+b_i)} \Big)^{-1}, \tag{A 4}$$

where dd is the bin spacing. The number flux density (NFD) per size class is analogous to the VFD per size class,

$$\dot{\mathcal{N}}(d_i) = \dot{\mathcal{G}}(d_i)/d_{ij}^3 = \frac{\pi}{6T_s\overline{\mathcal{A}}(1+b_i)} \sum_{j=1}^{N_i} 1. \tag{A 5}$$

Similarly, the NFD summed over all droplet classes is analogous to equation A 2,

$$\dot{n} = \dot{g}/d_{30}^3 = \sum_{i=1}^{D} \dot{\mathcal{N}}(d_i), \tag{A 6}$$

which allows that number flux density function is given by,

$$\mathrm{NFDF}(d_i) = \frac{\dot{\mathcal{N}}(d_i)/\mathrm{d}d}{\dot{n}} = \frac{1}{\mathrm{d}d} \sum_{j=1}^{N_i} \frac{1}{(1+b_i)} \Big(\sum_{i=1}^{D} \sum_{j=1}^{N_i} \frac{1}{(1+b_i)} \Big)^{-1}. \tag{A 7}$$

Note equation A 7 is mathematically the same as the PDF since the contribution of the probe area and integration time have been cancelled by the normalization. Thus, the NFDF is related to the VFDF by a simple transformation,

$$\mathrm{NFDF}(d_i) = \mathrm{VFDF}(d_i)(d_{30}^3/d_{ij}^3). \tag{A 8}$$

Appendix B. The mass flux-weighted diameter d_{43}

In A discrete (summation) notation was used to reflect how the calculations were performed numerically. If continuous (integral) notation is used the VFDF by definition gives,

$$\int_0^\infty \mathrm{VFDF}(d)\mathrm{d}d = 1. \tag{B 1}$$

The first moment of the VFDF is equal to the mass flux-weighted diameter d_{43},

$$d_{43} = \int_0^\infty d \ \mathrm{VFDF}(d) \ \mathrm{d}d. \tag{B 2}$$

This is verified by considering the discrete notation of this calculation,

$$d_{43} = \sum_{i=1}^{D} \sum_{j=1}^{N_i} \frac{d_{ij}^4}{(1+b_i)} \Big(\sum_{i=1}^{D} \sum_{j=1}^{N_i} \frac{d_{ij}^3}{(1+b_i)} \Big)^{-1}. \tag{B 3}$$

Acknowledgements

This work was sponsored by the Office of Naval Research (ONR), as part of the Multidisciplinary University Research Initiatives (MURI) Program, under grant number N00014-16-1-2617.

Declaration of Interests

The authors report no conflict of interest.

REFERENCES

ABKARIAN, M., MENDEZ, S., XUE, N., YANG, F. & STONE, H. A. 2020 Speech can produce jet-like transport relevant to asymptomatic spreading of virus. *Proc. Natl. Acad. Sci. U. S. A.* **117** (41), 25237–25245.

ALBRECHT, H. E., BORYS, M., DAMASCHKE, E. & TROPEA, C. 2003 *Laser doppler and phase doppler measurement techniques*. Springer Berlin Heidelberg.

BACHALO, W. D. 1994 Experimental methods in multiphase flows. *Int. J. Multiph. Flow* **20** (SUPPL. 1), 261–295.

BALACHANDAR, S., ZALESKI, S., SOLDATI, A., AHMADI, G. & BOUROUIBA, L. 2020 Host-to-host airborne transmission as a multiphase flow problem for science-based social distance guidelines. *Int. J. Multiph. Flow* **132**, 103439.

BROWN, G. L. & ROSHKO, A. 1974 On density effects and large structure in turbulent mixing layers. *J. Fluid Mech.* **64** (4), 775–816.

CHUNG, J. N. & TROUTT, T. R. 1988 Simulation of particle dispersion in an axisymmetric jet. *J. Fluid Mech.* **186**, 199–222.

DELON, A., CARTELLIER, A. & MATAS, J.-P. 2018 Flapping instability of a liquid jet. *Phys. Rev. Fluids* **3** (4), 1–20.

DIMOTAKIS, P. E. 1986 Two-Dimensional Shear-Layer Entrainment. *AIAA* **24** (11), 1791–1796.

DIMOTAKIS, P. E., MIAKE-LYE, R. C. & PAPANTONIOU, D. A. 1983 Structure and dynamics of round turbulent jets. *Phys. Fluids* **26** (11), 3185–3192.

DUMOUCHEL, C. 2008 On the experimental investigation on primary atomization of liquid streams. *Exp. Fluids* **45** (3), 371–422.

EATON, J. K. & JOHNSTON, J. P. 1980 Review of Research on Subsonic Turbulent-Flow Reattachment. *AIAA Pap.* **19** (9).

EATON, J. K. & JOHNSTON, J. P. 1982 Low Frequency Unsteadyness of a Reattaching Turbulent Shear Layer. *Turbul. Shear Flows 3* pp. 162–170.

ENGELBERT, C., HARDALUPAS, Y. & WHITELAW, J. H. 1995 Breakup phenomena in coaxial airblast atomizers. *Proc. R. Soc. Lond. A* **451**, 189–229.

EROGLU, H. & CHIGIER, N. 1991 Initial drop size and velocity distributions for airblast coaxial atomizers. *J. Fluids Eng. Trans. ASME* **113** (3), 453–459.

FAVRE-MARINET, M., CAMANO, E. B. & SARBOCH, J. 1999 Near-field of coaxial jets with large density differences. *Exp. Fluids* **26** (1-2), 97–106.

HARDALUPAS, Y, TAYLOR, A. M. K. P. & WHITELAW, J. H. 1989 Velocity and particle-flux characteristics of turbulent particle-laden jets. *Proc. R. Soc. Lond. A* **78** (1870), 185–195.

HARDALUPAS, Y, TAYLOR, A. M. K. P. & WHITELAW, J. H. 1990 Velocity and size characteristics of liquid-fuelled flames stabilized by a swirl burner. *Proc. R. Soc. London. A. Math. Phys. Sci.* **428** (1874), 129–155.

HARDALUPAS, Y & WHITELAW, J. H.W. 1993 Coaxial Airblast Atomizers. *Tech. Rep.*. Imperial College of Science and Technology.

HARDALUPAS, Y. H. & WHITELAW, J. H.W. 1994 Characteristics of sprays produced by coaxial airblast atomizers. *J. Propuls. Power* **10** (4), 453–460.

KUMAR, A. & SAHU, S. 2020 Liquid jet disintegration memory effect on downstream spray fluctuations in a coaxial twin-fluid injector. *Phys. Fluids* **32** (7), 073302.

LAMPA, A. & FRITSCHING, U. 2013 Large Eddy Simulation of the spray formation in confinements. *Int. J. Heat Fluid Flow* **43**, 26–34.

LASHERAS, J.C., VILLERMAUX, EMMANUEL & HOPFINGER, E.J. 1998 Break-up and atomization of a round water jet by a high-speed annular air jet. *J . Fluid Mech* **357**, 351–379.

LASHERAS, J. C. & HOPFINGER, E.J. 2000 Liquid Jet Instability nd Atomization in a Coaxial Gas Strea. *Annu. Rev. Fluid Mech.* **1** (1873), 406–459.

LAU, T.C.W. & NATHAN, G.J. 2016 The effect of Stokes number on particle velocity and concentration distributions in a well-characterised, turbulent, co-flowing two-phase jet. *J. Fluid Mech.* **809**, 72–110.

LAU, T. C. W. & NATHAN, G. J. 2014 Influence of Stokes number on the velocity and concentration distributions in particle-laden jets. *J. Fluid Mech.* **757** (6), 432–457.

LAZARO, B. J. & LASHERAS, J. C. 1992*a Particle dispersion in the developing free shear layer. Part 1. Unforced flow*, , vol. 235.

LAZARO, B. J. & LASHERAS, J. C. 1992*b Particle dispersion in the developing free shear layer. Part 2. Forced flow*, , vol. 235.

LING, Y., FUSTER, D., TRYGGVASON, G. & ZALESKI, S. 2019 A two-phase mixing layer between parallel gas and liquid streams: Multiphase turbulence statistics and influence of interfacial instability. *J. Fluid Mech.* **859**, 268–307, arXiv: 1808.01996.

LONGMIRE, ELLEN K. & EATON, JOHN K. 1992 *Structure of a particle-laden round jet*, , vol. 236.

LOZANO, A. & BARRERAS, F. 2001 Experimental study of the gas flow in an air-blasted liquid sheet. *Exp. Fluids* **31** (4), 367–376.

MACHICOANE, N., BOTHELL, J. K., LI, D., MORGAN, T. B., HEINDEL, T. J., KASTENGREN, A. L. & ALISEDA, A. 2019 Synchrotron radiography characterization of the liquid core dynamics in a canonical two-fluid coaxial atomizer. *Int. J. Multiph. Flow* **115**, 1–8.

MACHICOANE, N., RICARD, G., OSUNA-OROZCO, R., HUCK, P. D. & ALISEDA, A. 2020 Influence of steady and oscillating swirl on the near-field spray characteristics in a two-fluid coaxial atomizer. *Int. J. Multiph. Flow* **129**, 103318.

MARMOTTANT, P. H. & VILLERMAUX, E. 2004 On spray formation. *J. Fluid Mech.* **498** (498), 73–111.

MATAS, J.-P., DELON, ANTOINE A. & CARTELLIER, A. 2018 Shear instability of an axisymmetric air-water coaxial jet. *J. Fluid Mech.* **843**, 575–600.

MODARRESS, D., WUERER, J. & ELGHOBASHI, S. 1984 An experimental study of a turbulent round two-phase jet. *Chem. Eng. Commun.* **28** (4-6), 341–354.

MUNGAL, M. G. & HOLLINGSWORTH, D. K. 1989 Organized motion in a very high Reynolds number jet. *Phys. Fluids A* **1** (10), 1615–1624.

OSUNA-OROZCO, R., MACHICOANE, N., HUCK, P.D. & ALISEDA, A. 2019 Feedback control of coaxial atomization based on the spray liquid distribution. *At. Sprays* **29** (6), 545–551.

OSUNA-OROZCO, R., MACHICOANE, N., HUCK, P.D. & ALISEDA, A. 2020 Feedback control of the spray liquid distriubtion of electrostatically assisted coaxial atomization. *At. Sprays* **30** (1), 1–9.

PANCHAPAKESAN, N. R. & LUMLEY, J. L. 1993 Turbulence Measurements in Axisymmetric Jets of Air and Helium. Part 1. Air Jet. *J. Fluid Mech.* **246**, 225–247.

PICANO, F., SARDINA, G., GUALTIERI, P. & CASCIOLA, C. M. 2010 Anomalous memory effects on transport of inertial particles in turbulent jets. *Phys. Fluids* **22** (5), 1–4.

POPE, S.B. 2010 *Turbulent Flows*. Cambridge University Press.

PREVOST, F, BOREE, J., NUGLISCH, H. J. & CHARNAY, G. 1996 Measurements of Fluid/Particle Correlated Motion in the Far Field of an Axisymmetric Jet. *Int. J. Multiph. Flow* **22** (4).

REEKS, M. W. 1983 The transport of discrete particles in inhomogeneous turbulence. *J. Aerosol Sci.* **14** (6), 729–739.

REHAB, H., VILLERMAUX, E. & HOPFINGER, E. J. 1997 Flow regimes of large-velocity-ratio coaxial jets. *J. Fluid Mech.* **345**, 357–381.

SAFFMAN, P.G. 1965 The lift on a small sphere in a slow shear flow. *Fluid Mech.* **22**, 385–400.

SBRIZZAI, F., VERZICCO, R., PIDRIA, M. F. & SOLDATI, A. 2004 Mechanisms for selective radial dispersion of microparticles in the transitional region of a confined turbulent round jet. *Int. J. Multiph. Flow* **30** (11), 1389–1417.

TSO, J. & HUSSAIN, F. 1989 Organized motions in a fully developed turbulent axisymmetric jet. *J. Fluid Mech.* **203** (425), 425–448.

ÜNAL, A. 1989 Understanding liquid-jet atomization cascades via vortex dynamics. *Metall. Mater. Trans. B* **20B**, 61–69.

VILLERMAUX, E., MARMOTTANT, PH & DUPLAT, J. 2004 Ligament-Mediated Spray Formation. *Phys. Rev. Lett.* **92** (7), 1–4.

WYGNANSKI, I. & FIEDLER, H. 1969 Some measurements in the self-preserving jet. *J. Fluid Mech.* **38** (3), 577–612.

YODA, M., HESSELINK, L. & MUNGAL, M. G. 1992 The evolution and nature of large-scale structures in the turbulent jet. *Phys. Fluids A* **4** (4), 803–811.

YULE, A. J. 1978 Large-scale structure in the mixing layer of a round jet. *J. Fluid Mech.* **89** (3), 413–432.

ZALLER, M.M. & KLEM, M.D. 1995 Shear coaxial injector spray characterization. In *Liquid Rocket Engine Combustion Instability* (ed. V. Yang & W. Anderson), chap. 7, pp. 191–2. Washington, DC: American Institute of Aeronautics and Astronautics, Inc.

ZALLER, M. M. & KLEM, M. D. 1991 Coaxial Injector Spray Characterization Using Water/ Air as Simulants. *Tech. Rep.*. NASA.

ZANDIAN, A., SIRIGNANO, W. A. & HUSSAIN, F. 2018 Understanding liquid-jet atomization cascades via vortex dynamics. *J. Fluid Mech.* **843**, 293–354.